Accepted manuscript doi:
10.1680/jgeot.17.p.128

Submitted: 11 November 2017

Published online in 'accepted manuscript' format: 08 April 2019

Manuscript title: Modelling the seismic performance of root-reinforced slopes using the Finite Element Method

Authors: Teng Liang*, Jonathan Adam Knappett*, Anthony K. Leung*[†] and A. Glyn Bengough*[‡]

Affiliations: *Discipline of Civil Engineering, School of Science and Engineering, University of Dundee, Dundee, UK; [†]Department of Civil and Environmental Engineering, Hong Kong University of Science and Technology, Hong Kong SAR and [‡]The James Hutton Institute, Invergowrie, Dundee, UK

Corresponding author: Jonathan Adam Knappett, Discipline of Civil Engineering, School of Science and Engineering, University of Dundee, Dundee, UK.

E-mail: j.a.knappett@dundee.ac.uk

Accepted manuscript doi:
10.1680/jgeot.17.p.128

Abstract

This paper investigates the seismic performance of rooted granular slopes using dynamic finite element analysis, validated against recently published centrifuge test data. The importance of selecting suitable strength parameters to represent soil response within a strain hardening constitutive model was demonstrated and the simulations suggested that any boundary effects introduced through the use of the Equivalent Shear Beam container in the centrifuge are negligible and can be represented by a semi-infinite lateral boundary condition. Using the validated model, a parametric study investigated the effects of different rooted soil properties on the performance of slopes of different heights. Vegetation was effective in reducing deformations at the crest of modest height slopes, though the benefit reduced as slope height or soil apparent cohesion increased. The effectiveness was significantly affected by the extent of the root system, but only moderately sensitive to root cohesion, and insensitive to stiffness or damping of the rooted soil. Plant species possessing deep and extensive root systems are therefore recommended for seismic stabilisation rather than those with the strongest roots. For modelling purposes, it is sufficient to be able to quantify only the strength of the rooted soil and its area of influence. The magnitude of improvement from vegetation in terms of decreasing seismic permanent slip was also found to be insensitive to the construction method used (i.e. compacted/uncompacted embankment or cutting) for drained granular slopes.

Keywords: Slope stability; Earthquakes; Numerical modelling; Centrifuge modelling; Vegetation; Sands

Accepted manuscript doi:
10.1680/jgeot.17.p.128

1 Introduction

Numerical modelling using constitutive models of different levels of sophistication has been widely used for dynamic analysis of slope systems (e.g. Prevost *et al.*, 1985; Woodward & Griffiths, 1996; Elia *et al.*, 2011; Pelecanos *et al.*, 2013; 2015). These studies provided useful insights into ground motion propagation, topographical effects and hydrodynamic pressures within slopes through comparison with observations made from physical model tests and/or field measurements. However, most studies did not consider permanent slope deformation predominantly due to a lack of recorded deformation data. Al-Defae et al. (2013) and Knappett *et al.* (2015) suggested that the ability to capture soil permanent deformation accurately in numerical simulations is particularly important for considering the seismic performance of geotechnical systems over their design life, where behaviour in a future earthquake may be significantly affected by previous shaking.

The soil bioengineering method using vegetation is an ecologically and economically beneficial sustainable alternative to traditional civil engineering reinforcement techniques that have been widely incorporated for slope stabilisation in practice (e.g. Norris *et al.*, 2008; Wu, 2013; Stokes et al., 2009; 2014). Plant roots can improve slope stability mainly through direct mechanical reinforcement of soil (e.g. Wu, 1976; Pollen & Simon, 2005; Schwarz et al., 2010) and by modifying groundwater conditions by means of evapotranspiration (e.g. Smethurst et al., 2006; 2012; Leung & Ng, 2013; Boldrin et al., 2017). Some trials under laboratory conditions (e.g. Veylon et al., 2015) have been reported to directly quantify the relative magnitude of these two effects; however, such trials may over predict the hydrological effect as the detrimental consequences of vegetation in increasing soil infiltration was not considered (Simon & Collison, 2002; Leung et al., 2018). Sidle & Bogaard (2016) reviewed previous studies and indicated that the magnitude of the two effects varied by region and by the type of landslide. In temperate regions where storms that trigger shallow landslides occur during winter rainy seasons, soils are typically near field capacity and transpiration is minimal. The situation may differ in the tropics where transpiration modifies soil moisture year round. For shallow landslides, root reinforcement is a dominant stabilising agent while evaporation and transpiration play a minor role in landslide initiation. Conversely, evaporation and transpiration effects of evolving vegetation directly affect the movement of deep-seated landslides, with root reinforcement having only a minor influence.

Numerical simulation of the beneficial effects of roots on slopes has mainly focused on static or pseudo-static events, such as seasonal rainfall and establishment or clearance of vegetation. In terms of the mechanical effect, numerical simulations were generally conducted in one of two ways: (i) simulating the rooted zone as a zone of smeared properties, principally involving an additional cohesion c_r (measured in the field) added to the soil strength properties (e.g. Frydman & Operstein, 2001; Mao et al., 2014a; Temgoua et al., 2016), or (ii) treating roots as discrete beam or tensile anchor elements embedded into a soil continuum of finite elements (e.g. Lin et al., 2010; Bourrier et al., 2013; Mao et al., 2014b). The latter approach can be particularly computationally expensive, given the size of individual roots compared to the size of the slope. For the first approach, the root cohesion has generally been considered to be uniformly distributed along the slope surface. This may not be the case in the field, especially for tree- or shrub-rooted slopes at wider spacing. The main structure of a tree root system is typically concentrated within the ZRT (zone of rapid taper). Beyond this zone, roots may still extend to several metres, but the density will be relatively low and the reinforcing effect negligible (Gilman 1989; Schenk & Jackson 2002; Göttlicher *et al.* 2008). In terms of the hydrological effect of plants on slope stability,

Accepted manuscript doi:
10.1680/jgeot.17.p.128

numerical simulations have generally followed a two-stage process (e.g. Blatz et al., 2004; Leung & Ng, 2013; Ng et al., 2016): (i) the variation of pore water pressure (PWP) due to vegetation is calculated through a root water uptake model (e.g. Nyambayo & Potts, 2010; Jarvis, 2011) or prescribed according to field records; (ii) the calculated or prescribed PWP is then set as an input parameter for independent slope stability analysis. Precipitation and evapotranspiration rates have also been prescribed as boundary conditions (e.g. Tsiampousi et al., 2017).

Despite the attention paid to the study of rooted slopes under static conditions, a numerical investigation into the seismic response of rooted slopes subject to earthquake loading is relatively rare. Liang *et al.* (2015) developed a two-stage numerical model to quantify the performance of vegetated slopes subject to seismic motions: in the first stage, root soil interaction is quantified using a computationally-efficient macro-element by employing a beam-on-non-linear-Winkler-foundation (BNWF) approach using existing *p*–*y* formulations from piling engineering (Reese & Van Impe, 2011); the second stage defined equivalent continuum properties (e.g. additional representative cohesion) of a smeared zone representing the zone of rooted soil in a Finite Element analysis to simulate the global seismic response of the slope. This approach has been validated against idealised root groups of straight vertical rods. This may be a reasonable representation of a plate/heart root system where vertical or horizontal lateral roots grown from the main horizontal lateral roots or the base of the tree stem. For tap root systems, however, lateral roots are interlocked by the main tap roots. It should be noted here that Liang et al. (2015) isolated only the mechanical root reinforcement effects during earthquake events. This may be considered reasonable for coarse-grained soils as (i) the slip surface is generally shallow, such that evaporation and transpiration play a minor role in landslide initiation as mentioned above (after Sidle & Bogaard, 2016); (ii) root transpiration during an earthquake will be negligible due to the short duration of the event; and (iii) any beneficial effects on stability of lowering of the water table due to evapotranspiration can be negated by heavy rain prior to an earthquake; therefore, to ensure performance the hydraulic reinforcement effect cannot be relied upon, while the mechanical reinforcement will always be present. For a granular soil that is non-liquefiable (e.g. gravelly sand or sand with significant non-plastic fines content) the drained soil response will, therefore, be the critical case.

The aim of this paper is to use this numerical modelling technique for application to slopes reinforced by deep taproot systems representative of realistic 3-D root architectures when subject to seismic ground motion. The numerical model will be validated against the database of centrifuge tests reported by Liang & Knappett (2017b), as summarised in Table 1. These tests involved the use of an Equivalent Shear Beam (ESB) container at modest model scaling factors (based mainly on root size considerations) such that the slope toe and crest were relatively close to the container boundaries. These boundary conditions will be modelled in detail and compared to an extended soil boundary condition for application to field cases that has been conventionally adopted when back-analysing dynamic centrifuge tests (e.g. Al-Defae *et al.*, 2013). After validation of the approach, a parametric study will investigate the influences of different potential continuum properties of rooted soil on the overall seismic performance (slip and crest acceleration) of rooted slopes of different heights, soil parameters, slope angles and construction techniques.

2 Finite element modelling

Two–dimensional plane-strain numerical simulations were conducted using the commercial finite element program PLAXIS 2D 2015. Typical numerical models of rooted slopes (1:30

Accepted manuscript doi:
10.1680/jgeot.17.p.128

scale slope) are shown in Fig. 1(a). Two different approaches to modelling the boundary conditions were considered: (i) extension of both the left and right boundaries to represent a semi-infinite soil condition with an absorbent boundary (as indicated in Fig. 1(a)); and (ii) modelling the ESB container explicitly (Fig. 2). In the first case, absorbent boundary conditions (Lysmer & Kuhlemeyer, 1969) were applied on both sides. Such a boundary can be described by two series of dashpots oriented normal and tangential to the boundary of the FE mesh. One of the concerns with using such viscous boundaries is that for low frequency excitations in multiple directions it may lead to permanent displacements even in an elastic system (e.g. Kellezi, 2000 ; Kontoe et al., 2009). However, only absorption of body waves in the *x*-direction was considered in this study. Modelling the mechanical behaviour of the ESB container for the latter case will be described in detail in the following section.

After the slope geometry was configured (including assigning appropriate constitutive properties to different zones), the initial stress state was generated by turning the gravity loading on, with the lateral earth pressure coefficient input as a model parameter, where $K_0 = 1-\sin\phi'$. Earthquake ground motion was input in the time domain along the bottom boundary of each model (as indicated by the arrows in Figs. 1 and 2). The waveform used in each case was a displacement time history a time step of 0.016 s obtained from integrating the acceleration record measured at the bottom of the centrifuge model slopes, with appropriate high pass filtering between integration stages. Each model was subjected to eight successive earthquake motions, comprising three different historical records with distinct peak ground acceleration (PGA), duration and frequency content, as shown in Fig. 3. The first motion (EQ1) was recorded during the 1995 Aegion earthquake (M_s 6.2). This was followed by three nominally identical stronger motions (EQ2 – EQ4) recorded from the 1994 Northridge earthquake (M_s 6.8), three (EQ5 – EQ7) from the 2009 L'Aquila earthquake (M_s 6.3), and finally, a repeat of the Aegion motion (EQ8). The Newmark implicit scheme was employed to perform time integration within the simulations. Two coefficients α and β, which control the accuracy of the numerical time integration were set to be 0.25 and 0.5 in this study, respectively, to maintain a stable solution.

2.1 Modelling the behaviour of the ESB container

2.1.1 General consideration

The numerical model adopted to discretely model the behaviour of the ESB container is shown in Fig. 2 (fallow soil condition shown). Here, the dimensions of the slope were established based on the actual prototype size of the centrifuge model. The soil model was simulated using 15-node triangular elements. Such elements provide fourth-order integration for displacements and the numerical integration involves twelve Gauss points. A very fine mesh (500-1500 elements, the exact number depending on the slope geometry and local refinement in the rooted zone) was defined. All soil materials were simulated using the Hardening Soil constitutive model with small-strain stiffness (Schanz et al., 1999). Parameter selection for this material will be discussed later. The ESB container was simulated using 5-noded plate elements mimicking the layered structure of the ESB container which consisted of 6 aluminium frames and 5 rubber inter-layers. The behaviour of the plate elements follows Mindlin's theory (Bathe & Saunders, 1984), which allows for plate deflections due to shearing and bending. Rotational fixity was applied to the bottom of each plate to fix the rotational degree of freedom and thereby account for the thickness of the container walls in minimising rotation. Node-to-node anchors, which did not interact within the soil were used to connect the plate elements at a given elevation on either side of the container to represent the solid aluminium rings by constraining the horizontal deformations of the two end walls to

Accepted manuscript doi:
10.1680/jgeot.17.p.128

be identical. Interface elements were assigned between the soil and the ESB container walls to simulate the frictional condition between them. The interface was set to be fully rough to ensure that the end walls had the same stress distribution as the adjacent soil (as in the ESB - see Zeng & Schofield, 1996).

2.1.2 Material properties

Both the aluminium and rubber plate elements were modelled as isotropic elastic materials with six input parameters: axial stiffness *EA*; bending stiffness *EI*; specific weight *w*; Poisson's ratio *v*; and two viscous (Rayleigh) damping ratio parameters c_m and c_k. All plate parameters used are summarised in Table 2 and Table 3. The rubber layers were simulated as an isotropic elastic material with an absorbent boundary applied to the end walls.

The shear modulus of the rubber layer (G_{rubber}; in kPa) used in this study was taken as:

$$G_{rubber} = 1374 + 14.6 \cdot \sigma_v \qquad (1)$$

after Bertalot (2013), where the normal stress on the rubber σ_v represents that induced by the weight of the aluminium frame(s), and therefore varies with working *g* level in the centrifuge and with an elevation of each layer within the container. The Young's Modulus of the rubber ($E_{rubber;}$ in kPa) was then derived from the following elastic relationship:

$$E_{rubber} = 2G_{rubber}(1 + \upsilon_{rubber}) \qquad (2)$$

where v_{rubber} of the rubber was set to be 0.5. For the plane-strain model, the value of *EA* (kN/m) relates to stiffness per unit width in the out-of-plane direction, calculated by

$$E_{rubber} A = E_{rubber} \cdot d_{eq} \cdot 1m \quad (3)$$

where d_{eq} is the equivalent width of the rubber sheet over the whole layer (0.375m at the prototype in this study). The bending stiffness *EI* (kN m^2/m) was estimated as a function of *EA* and d_{eq}:

$$d_{eq} = \sqrt{12 \frac{E_{rubber} I}{E_{rubber} A}} \qquad (4)$$

The weight of the rubber was considered to be negligibly small compared to the weight of the aluminium layers and was therefore taken to be zero. The viscous damping of rubber was approximated as 5% according to Vince & Askenazi (1999). This value was applied as the Rayleigh damping at the input frequency range. Details on the determination of appropriate damping coefficients (c_m and c_k) can be found in Section 3.1.

The Young's Modulus E_{Al} and Poisson's ratio v_{Al} of the aluminium were taken from Eurocode 9 (BSI, 2007). The corresponding stiffness properties were then determined in the same way as for the rubber (see Eq (2) and Eq (3)). For the node-to-node anchors that connect the two end walls at each layer, the axial stiffness was set to match the axial stiffness of the long edges of the aluminium frames, as measured from compression tests of the aluminium rings in an Instron load frame (Bertalot, 2013). The weight w_{Al} of the aluminium frame elements were set to represent the actual measured weight of an individual frame as reported by Bertalot (2013). The viscous damping of the aluminium frame was taken to be 0.04% after Vince & Askenazi (1999).

2.1.3 Boundary conditions

A modified absorbent boundary was applied to the inner surface of the end walls to approximate the hysteretic energy dissipation in the rubber due to the hyperelasticity of the material response that cannot be captured implicitly by the linear elastic idealisation used.

Accepted manuscript doi:
10.1680/jgeot.17.p.128

The normal and shear stress components absorbed in the *x*-direction may be expressed as (Lysmer & Kuhlemeyer, 1969):

$$\sigma_n = -C_1 \rho V_P v_X \qquad (5)$$

$$\tau = -C_2 \rho V_S v_y \qquad (6)$$

where ρ is the density of the soil, v_X and v_y are the velocities of a volume; V_P and V_S are the pressure wave velocity and shear wave velocity, respectively, and can be determined by

$$V_P = \sqrt{\frac{E_{oed}}{\rho}} \qquad (7)$$

$$V_S = \sqrt{\frac{G_0}{\rho}} \qquad (8)$$

where C_1 and C_2 are relaxation coefficients which control the amount of energy absorption. A perfectly absorbent boundary is achieved if $C_1 = C_2 = 1$, which represents the case for the semi-infinite soil boundary condition (Fig. 1). As indicated by Zeng & Schofield (1996), the ESB design philosophy prioritises avoiding S-wave reflection by tuning of the container dynamic properties. Additionally, it was assumed that any missing rubber damping would manifest as unwanted P wave reflection, so C_2 was initially set to be 0. After several attempts, using $C_1 = 0.4$ and $C_1 = 0.2$ was able to match the dynamic acceleration response within the soil body as measured in the centrifuge for the 1:10 scale model and 1:30 scale models, respectively.

2.2 Constitutive modelling of soil

The dry HST95 silica sand was simulated using the Hardening Soil constitutive model with small-strain stiffness ('HS Small', Schanz et al. 1999). The stress- and strain-dependent elastic part of the model was derived from the strain-dependent stiffness model proposed by Santos & Correia (2001):

$$\frac{G}{G_0} = \frac{1}{1 + 0.385\left|\frac{\gamma}{\gamma_{0.7}}\right|} \qquad (9)$$

where $\gamma_{0.7}$ is the shear strain at which the secant shear modulus G has reduced to 70% of its initial value (G_0).

Plastic behaviour of the soil is represented using a cap-type yield surface for volumetric hardening combined with a non-associative Mohr-Coulomb failure criterion for deviatoric hardening. Strain softening behaviour was not modelled. Al-Defae et al. (2013) suggested using the critical-state friction angle ($\phi' = \phi'_{crit}$) in unreinforced cases with large shear deformations that accrue rapidly in granular slopes during strong earthquake shaking. Given that the reinforced slopes considered here may not displace as far, ignoring any soil dilation influence on strength might result in a significant over-prediction of deformations (Bolton & Take, 2011). In order to address this issue, three different sets of shear strength properties were considered in the initial validation: case (a) critical-state friction angle ϕ'_{crit} and zero dilation; case (b) peak friction angle ϕ'_{pk} and the corresponding dilation angle; case (c) an equivalent friction angle ϕ'_{eq} that falls between the peak and critical state values and the corresponding dilation angle. The value of ϕ'_{pk} was determined as a linear function of relative density I_D, over the stress range considered (after Al-Defae *et al.*, 2013):

$$\phi'_{pk} = 20I_D + 29 \qquad (10)$$

The dilation angle (ψ') was calculated using the following equation (Roy & Campanella, 1996),

$$\sin\psi' = \frac{\sin\phi' - \sin\phi'_{crit}}{1 - \sin\phi'\sin\phi'_{crit}} \qquad (11)$$

The equivalent friction angle ϕ'_{eq} was given by

$$\phi_{eq}{}' = \phi'_{crit} + k(\phi'_{pk} - \phi'_{crit}) \qquad (12)$$

where k is a reduction factor; $k = 0$ implies critical state strength; $k = 1$ implies peak strength; otherwise, $0 < k < 1$. Based on a series of isotropically consolidated drained triaxial tests of fully saturated samples sheared at different effective confining pressures at an initial relative density of 50%, the value of k was calibrated to be 0.5. After extensive shearing, the soil was expected to arrive at a critical-state void ratio (e_{crit}), where dilation ceases. For HST95 silica sand, e_{crit} was taken to be 0.717 over a range of effective confining stress from 1 to 100 kPa (based on data from Lauder, 2010).

The parameters used are summarised in Table 4. Damping will be discussed further during validation against the centrifuge test data for the fallow slopes (below).

2.3 Modelling of root-soil mechanical interaction

A simplified modelling method was adopted to capture the mechanical root-soil interaction. In each numerical model, rooted soil zones were defined (see Fig. 1), which were assumed to have the same mechanical properties as the surrounding soil, but with an additional smeared 'root cohesion' added to the HST95 soil properties, for the purposes of validation. The additional shear strength with depth within the centrifuge models was determined by considering different potential slip depths and performing a series of tests within a large direct shear apparatus (DSA) on the 3-D printed root models in HST95 sand of the same density and with confining effective stresses applied to be representative of that in the centrifuge model at the shear plane location (see Fig. 4(a)). It should be noted that these tests are only indicative of the rooted soil shear strength at different depths within the centrifuge models as the trend of increasing confining stress with depth in the centrifuge tests could not truly be simulated within the DSA, as demonstrated in Fig. 4(a).

Root clusters were uniformly distributed by a spacing S of 1.4 m in the longitudinal direction of the 3-D slope in the centrifuge, so that the equivalent (smeared) area, A_s, of shear plane per metre length of the slope over which the additional root strength acts in the 2-D plane strain FE models is given by

$$A_s = r \cdot S \qquad (13)$$

where r is the radius of the 3-D root cluster, following Liang *et al*. (2015). The values of root cohesion measured in the field are around several kPa and seldom higher than 20 kPa (see database collected by Schmidt et al., 2001; Wu, 2013; Liang et al. 2017a). Hence, the root cohesion values used in this study (see Fig. 4(b)) are representative of field measured values.

3. Validation of numerical model

3.1 Determination of appropriate damping parameters

Recent previous validations of FE models against centrifuge test data for this centrifuge, soil and container have used the semi-infinite lateral boundary approach, and have indicated that

Accepted manuscript doi:
10.1680/jgeot.17.p.128

there is a small amount of additional viscous damping required to correctly model the measured hysteretic behaviour of the sand in terms of its stress-strain and damping response (see Amorosi *et al.*, 2010, Al-Defae *et al.*, 2013, Knappett *et al*., 2015 and Liang *et al.*, 2015). This is principally to remove unwanted oscillations outside the range of the input frequency. In order to perform a similar soil property calibration here that can be compared to these previous studies the amount of additional viscous damping required was determined using the model geometry shown in Fig. 1. Rayleigh damping, which allows additional mass and stiffness-proportional damping to be modelled, was added to the soil material, as given by:

$$\zeta_{add} = c_m \left(\frac{1}{4\pi f_n} \right) + c_k (\pi f_n) \quad (14)$$

where ζ_{add} is the additional equivalent viscous damping ratio, f_n is the natural frequency of modes within the soil, and c_m and c_k are the mass and stiffness proportional damping constants, respectively. The additional damping values required to achieve a good match between the numerical simulations and the centrifuge results (in terms of inferred shear modulus and overall damping inferred from individual stress-strain loops, accelerations and crest deformation) are listed in Table 5. The additional damping was applied as a range bounded by $\zeta_{\max} = \zeta_{desired} + \Delta$ and $\zeta_{\max} = \zeta_{desired} - \Delta$ within the input motion frequency range (f_{min} to f_{max}), as shown in Fig. 5. Full details about the determination of the values of damping ratio bounds can be found in Hall (2006).

It was found that for slopes subject to similar earthquake motions (i.e. same lower cut-off frequency), a slightly higher additional viscous damping was required for the taller slope (2.5%, 7.2m height for test TL 08) compared to the shorter slope (1.5%, 2.4 m height for test TL 04). For the same given 7.2 m height slope subject to motions with different frequency content, a higher additional viscous damping was required for the case with greater low frequency content (3%, 1.33-10Hz for test TL05) compared to the reduced frequency case (2.5%, 4-10 Hz for test TL 08). The same damping ratio was used for both the rooted and fallow zones of soil within the validation simulations (it will be demonstrated later in the parametric study that changing the amount of damping in the rooted zones compared to the surrounding soil has a negligible effect on the response).

A comparison of the measured and simulated accelerations at the crest of the slope for test TL 05 in and the frequency domains is shown in Fig. 6. The accelerations (in terms of the envelope of the peak values for the FEM simulations) without applying any additional damping were significantly over-predicted in places, but those with additional viscous damping of 3% (in this case) showed a much improved match with the centrifuge measurements.

3.2 Determination of appropriate shear strength parameters

The effects of using the different sets of soil shear strength parameters on the permanent slope crest settlement for simulating the 7.2 m fallow slopes (TL 04, TL 05 and TL08) across the eight earthquakes are shown in Fig. 7. As expected, the use of peak strength parameters (case (b)) under-predicted the measured crest settlement in all cases. A significant over-prediction was found when using the critical-state strength parameters (case (a)), for the 7.2 m slope both under large motions (TL 05) and small motions (TL 08), while the use of equivalent shear strength parameters (case (c)) resulted in a good match with the centrifuge measurements. Corresponding shear stress-strain loops at mid depth between centrifuge tests and numerical simulation is shown in Fig. 8. Here the data points were determined from second-order estimates using the accelerometer array at the crest of the slope following the

Accepted manuscript doi:
10.1680/jgeot.17.p.128

method proposed by Brennan et al. (2005). As shown in Fig. 8, FEM provided a quite reasonable representation of soil dynamic response in terms of stress-strain response and the implicit stiffness.

Since case (c) gave the best match with the centrifuge observations, this set of strength parameters were used in the corresponding rooted slope cases to evaluate the effectiveness of the modelling of the mechanical soil-root interaction using the "smeared"-zone approach with only additional 'root cohesion'. Fig. 9 shows a comparison of the measured and simulated time histories of permanent crest settlement in the 1:30 rooted slopes. This demonstrates that simulating the rooted zone with this highly simplified approximation is effective.

3.3 ESB container boundary effect

Fig. 10 shows a comparison of the acceleration response (acceleration response spectrum near the crest for EQ2) and the permanent slope crest settlement for the FE simulations of the ESB container and semi-infinite lateral boundary cases for the 1:30 fallow slope (TL 05). Case (c) strength parameters were used as identified in the previous section. It can be seen that any boundary effect of the container end walls on the dynamic response of the soil was small (Fig. 10(a)). Simulations with the ESB modelled explicitly resulted in slightly larger permanent deformations (by approximately 10%) than those modelled by using a semi-infinite soil boundary condition, mainly resulting from a difference during the first earthquake. This is mainly attributed to the relative stiffness between the ESB container and the soil layer as suggested by Zeng & Schofield (1996). At smaller strains (EQ1), the shear stiffness of the soil layer will be higher than that of the container walls (which were tuned during design for a lower soil stiffness). As a result, the deformation of the walls will be slightly larger than that of the soil, such that the model container would drive the soil to deform slightly further, hence leading to a slightly higher crest settlement. During the subsequent motions, with the accumulation of shear strain, the shear stiffness of the soil drops to a value that is closer to that of the end walls, so this difference does not generally grow larger in the subsequent stronger motions as the deformations of the container walls and soil are more consistent. There is, however, some over-prediction of both simulations later in the sequence which may be due to soil densification introduced by the previous shaking in the centrifuge soil, which was not considered via a phased change of input properties between earthquakes during the FE modelling.

Considering the negligible difference for the overall deformation between the two approaches to modelling the boundary conditions, the semi-infinite lateral boundary method was used in the subsequent parametric study so as to highly reduce the computational time and physical memory required for the computations.

4. Parametric study

Using the validated numerical model, a parametric study was conducted to provide further insights into the selection of smeared zone properties for representing the rooted soil zones, and the effectiveness of roots as a performance-improving remedial technique for slopes of different heights and gradients, different construction technique, both in cohesionless (I_D = 57%) and c'-ϕ' soil. The rooted zone parameters varied included: (a) reduction of root cohesion to simulate the earthquake sequence striking when the slope has a weaker/younger root system or root ageing/decay; (b) the effect of reduced or increased damping of the soil-root matrix compared to that of the surrounding soil; (c) the effect of reduced or increased stiffness (shear modulus) of the soil-root matrix compared to that of the surrounding soil; and

Accepted manuscript doi:
10.1680/jgeot.17.p.128

(d) the width of the zone over which the root cohesion acts (i.e. the effect of root lateral spread/extent). In each analysis, different slope heights (ranging from 2.4 to 12 m, covering a wide range of common heights for infrastructure embankments/cutting slopes) but having the same root depth of 1.5 m were considered and were subject to identical motions taken from test TL 06 (which have the fullest frequency content). Rooting depth of 1.5 m was selected because it is the prototype value of the root cluster used in all the centrifuge tests used for validation in this study. In the field, although most species can have roots up to/longer than 2 m, more than 90% of root biomass is typically found in the top 1.5 m of soil (e.g. Jackson et al., 1996; Canadell et al., 1996; Schenk & Jackson, 2002). Higher viscous Rayleigh damping ratios were applied for taller slopes (see Fig. 11) to approximately capture this apparent effect which was observed during validation. To quantify any changes to slope performance due to these various parameter changes, the ratios of the displacement and peak ground acceleration (PGA) at the crest of the rooted slope to those of the fallow slope were defined in each case. The lower these ratios, the greater effect the roots will have in reducing seismic slope deformation and topographic amplification.

4.1 Effect of rooted soil strength

The effect of lower root cohesion at the time of the earthquakes is shown in Figs. 12(a) and 13(a). In this part of the parametric study, the magnitude of root cohesion at all depths in Fig. 4(b) was reduced proportionally by the reduction factor shown on the *x*-axis of these figures. Normalised cohesion of 1.0 means that root resistance is equivalent to that tested in the centrifuge (values as shown in Fig. 4). It is immediately apparent that in terms of permanent deformation, the roots are much more effective in shorter slopes. In all cases, there is a negligible increase in settlement even with a reduction in root cohesion by 50% (for shorter slopes, the settlement reducing effect is largely maintained even for 75% reduction, i.e., up to approximately 4~5 kPa of root cohesion at mid depth within the rooted zone and 2-3 kPa below 1 m depth). This suggests that root systems considerably weaker than the one considered during the centrifuge testing will also be effective in reducing seismic deformation and is consistent with a previously proposed mechanism of the performance improvement resulting from the zone of intense shear being deviated deeper, beneath the rooted zones (Liang & Knappett, 2017a), and that a relatively modest amount of root cohesion is required to achieve this. For taller slopes, the rooted zone is smaller in depth relative to the slope height, so the zone of intense shear is deviated proportionally less compared to the position in the corresponding fallow slope, resulting in a reduced proportional reduction in settlement. These results are also important in terms of the long-term management of vegetated slopes because root strength decays gradually, rather than abruptly, as plants die (Preti, 2013; Vergani *et al.*, 2014). The PGA at the crest is not sensitive to reduced root cohesion within the rooted zones (see Fig. 13(a)), regardless of the size of the slope being considered. This is thought to be because vertically propagating shear waves can effectively bypass the rooted zones.

4.2 Validity of neglecting stiffness and damping changes within rooted soil

In modelling the rooted soil zones in the earlier validation exercise, the underlying stiffness properties and damping were unaltered in rooted zones compared to the surrounding fallow soil. Figs. 12(b) and 13(b) show the influence of reducing or increasing the damping in the rooted soil zone only (where $\zeta_r/\zeta_s = 1$ implies rooted and fallow soil have the same damping properties, as assumed during validation). It can be seen that the slope crest settlement is not sensitive to the damping within the rooted zones, regardless of the height of the slope being

Accepted manuscript doi:
10.1680/jgeot.17.p.128

considered. This is consistent with the ground motion amplitude also not being affected by rooted zone damping (Fig. 13(b)).

Figs. 12(c) and 13(c) show the influence of reducing or increasing the stiffness properties in the rooted soil zone only (where $G_r/G_s = 1$ implies rooted and fallow soil have the same stiffness properties, as assumed during validation). All stiffness properties (G^{ref}, E_{oed}^{ref}, E_{50}^{ref} and E_{ur}^{ref}) within the constitutive model were reduced or increased proportionally. It would be expected generally that the addition of roots would increase the stiffness of the rooted zone (Liang *et al.*, 2015; Wood *et al.*, 2016); however this is shown to have a negligible effect on the crest settlements and accelerations for all slope heights. The repeated growth and death of roots in soil has the potential to break up the soil in the rooted zone, lowering its density and stiffness. If this was to occur, then the maximum possible reduction from a soil at $I_D = 100\%$ to $I_D = 0\%$ around the roots would only be of the order $G_r/G_s \approx 0.5$ (see relationships in Table 4). From Fig. 12(c) and 13(c), this would imply that in shorter slopes, even such an extreme alteration to soil density due to root action would have a negligible effect on settlement reduction and ground motion amplitude at the crest. However, the effect does increase in significance for taller slopes in terms of permanent deformation (the small 15% reduction for a 12 m high slope would be approximately halved, Fig. 12(c)).

In combination, it appears that it is valid to model the effect of roots by a change (increase) in shear strength only and to use the stiffness and damping of fallow soil for the rooted case.

4.3 Influence of lateral extent of rooted zone

For different plants of the same species, the lateral extent of the root system may vary when the plant grows e.g. the roots may spread over a reduced distance laterally but go deeper in search of water. Starting from the lateral extent of the rooted zones shown in Fig. 1, the width of the zone was reduced, reducing the area of the shear plane within the rooted zone, while the cohesion was kept the same, thereby representing the same root area ratio (RAR) and distribution of strong and weak roots within this zone. Fig. 12(d) indicates that as the rooted zone becomes narrower, the settlement reduction effect by roots becomes smaller ('Normalised root area' represents the multiplication factor on the width of the rooted zone used in the validation). In combination with the effects noted for lower root cohesion (Fig. 12(a)), this suggests that it may be advisable to select plant species for their propensity for lateral spread and deep rooting, rather than species with the strongest possible roots, to maximise the settlement reducing effects of the vegetation. This also has important implication for field measurement of rooted soil properties, as it would appear to be desirable to use rapid tests that measure only strength properties, but which can do this in many locations in a short period of time, rather than a smaller number of highly detailed tests (e.g. in-situ direct shear tests). Such devices are currently under development (e.g. Meijer *et al.*, 2016; 2018). As for the other parameters described previously, changes in the lateral extent of the rooted zone have a negligible effect on ground accelerations at the crest (Fig. 13(d)).

4.4 Effect of slope construction technique on effectiveness of root reinforcement

Previous studies (e.g. Potts et al., 1990; 1997) have shown that the soil stress state after construction can be different between embankments and cuttings due to the different soil loading paths followed, even where these slopes are formed by the same type of soil material. By using the validated FE model, further parametric study was conducted to evaluate whether the construction-induced initial soil stress state would alter the effectiveness of the root reinforcement, as compared to the "gravity turn-on" case experienced in the centrifuge.

Accepted manuscript doi:
10.1680/jgeot.17.p.128

Additional simulations were undertaken on slopes using the same rooted zone properties as the centrifuge tests (i.e. 100% normalised root cohesion cases; see Section 4.1) but modelling different pre-earthquake construction techniques.

Two types of embankment were considered, namely, a compacted embankment and an end-tipped (uncompacted) embankment (Skempton, 1996). For the compacted embankment cases, after establishing the initial stress field in the level ground (Part A, see Fig. 1(b)), construction was subsequently modelled by activating an additional soil layer above and applying a uniform vertical pressure, followed by its removal. The magnitude of compaction pressure selected was 150kPa, based on in-situ compaction test data on gravelly sand (Mooney & Rinehart, 2009). This process of activation-loading-unloading was continued, layer-wise, until the embankment was complete. The thickness of each layer was 1.2 m, which was determined as a compromise between computational efficiency and approximating field methodologies (where lift thickness between 0.1-0.8m may typically be used, depending on the compaction method and compaction plant selected (Highways Agency, 2016)). The discrete 'steps' resulting from this process were subsequently removed by deactivating a triangular wedge in each case to leave the final finished slope surface (Part C in Fig. 1(b)). The rooted zones were then changed from soil properties to those of rooted soil, before the earthquake sequence was finally simulated.

For the end-tipped (uncompacted) embankment and cutting cases, after establishing the initial stress field in the level ground, construction or excavation was simulated by activating the soil mass layer by layer (see Fig. 1(c)), or deactivating the excavated zone in several stages (see Fig. 1(d)), respectively, until the shape of the slope was established. The rooted zones were then changed from soil properties to those of rooted soil, before the earthquake sequence was simulated. The thickness of each soil layer for these cases was also taken as 1.2 m.

Comparison of the initial vertical and horizontal stress contours after construction but before earthquake excitation among the four cases is shown in Fig. 14, all for 1:2, 4.8 m high slopes. The main differences in the stress field are associated with the horizontal effective stresses, particularly for the compacted embankment case. Fig. 15 shows the variation of horizontal stress with soil depth at different positions within the slope (markers indicate the position of instrumentation within centrifuge tests), with limiting lateral earth pressures marked for reference. For the compacted embankment case, the lateral earth pressures are much higher than the other three cases, which are similar, and evidence of the mobilised lateral earth pressure coefficient reducing at depth is also observed, (as measured in field and laboratory compaction, e.g. Ingold, 1979; Duncan & Seed, 1986; Chen et al., 2008).

From Fig. 16, the influence of roots on the seismic slope performance (in terms of permanent deformation of the slope crest and crest peak acceleration) appears to be insensitive to the variation of initial stress associated with the different construction techniques, at least for the ground conditions considered herein. It should be noted that the absolute permanent deformations of the fallow slopes were significantly different in magnitude between the different construction methods. However, a similar effect was also observed for the rooted cases, resulting in improvement factors which are of similar magnitude in all cases (Fig. 16)

4.5 Effect of soil cohesion on root influence

Some apparent soil cohesion may be observed in granular soil materials forming slopes as a result of a significant fines content (e.g. some silt) or cementation (Coop & Atkinson, 1993). A cutting case was considered in this section, in which the soil cohesion was increased to 5

Accepted manuscript doi:
10.1680/jgeot.17.p.128

kPa from the nominal value in Table 4. The input cohesion values for the rooted soil at all depths were the sum of this apparent soil cohesion and the root cohesion from Fig. 4. Two cases were considered here: (i) 1:2 slopes of varying heights (as before), resulting in increased static factor of safety (FOS) and dependence of this on slope height; and (ii) keeping the static FOS the same as in the cohesionless 1:2 slopes under fallow conditions by varying the slope angle (1:0.65, 1:1.07, 1:1.29, 1:1.41 and 1:1.49 for the 2.4 m, 4.8m, 7.2m, 9.6m and 12 m slope, respectively). In both cases, the rooted zones were arranged at a constant horizontal centre-to-centre spacing of 2.4 m (in plane, between toe and crest) with the centreline of the first rooted zone 1.2 m away from the crest of the slope in the horizontal direction (see Fig. 1(a)). As a result of this, there was insufficient space for the 1:0.65 (β = 57°), 2.4 m slope to fit one entire root system and hence no simulations for this situation were conducted. Static FOS values are shown in Fig. 17(a) and these were calculated using the shear strength reduction method (Griffiths & Lane, 1999).

From Fig. 17(b) it appears that roots are also effective in slopes with a small amount of apparent soil cohesion, though less effective than in the cohesionless case. This is possible because the fallow zone of intense shear is deeper with increasing cohesion, resulting in a lower proportional change from the zone of intense shear being deviated below the rooted zone. However, by increasing the static FOS, the yield acceleration of the slopes with cohesion will be higher and so they will require stronger motions to cause slip. It should be noted that the pattern of increased effectiveness in shorter slopes appears to be similar. This is also true of the cases with variable slope angle, where it appears that by designing statically to a target FOS (1.5-1.6 in this case), the effectiveness of the roots will be similar to the cohesionless case (as the yield accelerations will likely be similar). The normalised PGA values at the crest are shown in Fig. 17(c) and are close to 1.0, which clearly suggest that the insensitivity of the response parameter to root presence also applies in slopes of different angle and soil properties.

5 Conclusion

In this paper, the ‘smeared property’ modelling approach for Finite Element simulation of rooted soil proposed initially by Liang *et.al* (2015), has been validated against a wider database of recently published centrifuge test data for vegetated coarse-grained non-liquefiable slopes under earthquake shaking. This covers situations in which the root architecture is more representative and where slope height is a variable. The influence of selecting suitable mobilised strength parameters for a strain-hardening constitutive model was investigated, along with verification that the ESB container used in the centrifuge tests was closely representative of a semi-infinite lateral boundary condition. Following this detailed validation, an extensive parametric study was conducted to investigate the influence of different potential characteristics of rooted soil on the overall seismic performance of slopes of different heights geometry and construction, broadly representative of those used in infrastructure embankments/cuttings. The following principal conclusions can be drawn from this study:

1) It was demonstrated that the effect of the roots within an FE model could be approximated by an increase in apparent cohesion in the rooted zone only; changes to the soil stiffness or damping in the rooted zones had a generally negligible effect on the slope performance (though if soil is reduced in density due to disturbance during root growth, a small reduction in the effectiveness of the roots may be observed).
2) The presence of zones of rooted soil on the slope face were found to significantly reduce crest settlements in cohesionless sandy 1:2 slopes of shorter height (reductions

of the order of 80% for a 2.4 m high slope were observed), but were less effective as the slopes became taller (reduction of the order of 20% for a 9.6 m high slope). Roots were also found to be similarly effective in slopes with a small amount of apparent soil cohesion and with different slope angles.

3) Roots appear to be less effective in slopes having a higher fallow static factor of safety, but as such slopes are more stable and will therefore have smaller deformations during earthquake shaking (higher yield accelerations), they are less likely to have to rely on the effects of roots to improve performance.
4) The performance improvement due to the vegetation (in terms of permanent deformations) was found to be significantly influenced by the horizontal extension of the root system. Lower values of root cohesion, (e.g. species with weaker roots or due to root decay) resulted in a negligible change in the settlement reducing effect at all slope heights for root cohesion reductions down to 50% of the value tested in the centrifuge. This implies that slopes may gain the full benefit of the roots even when they are not yet fully developed, or when they have started to decay substantially, given typical values of root soil strength observed in previous field studies.
5) The magnitude of improvement of crest permanent deformation due to the vegetation was found to be insensitive to the construction methods of the drained granular slopes considered.
6) The findings outlined in point (3) suggest that selection of species to optimise root depth and spread is potentially more important than selecting for roots which are the strongest biomechanically. This suggests that the further development of new rapid in-situ rooted soil strength assessment techniques that can define the extent of the strengthened rooted zone is to be encouraged.

ACKNOWLEDGEMENTS

The authors would like to express their sincere gratitude to Shengwenjun Qi and Xingyu Zhang at the University of Dundee for their assistance in performing some of the numerical simulations. The first author would like to acknowledge the financial support of the China Scholarship Council.

NOTATION

A	cross-sectional area
A_s	equivalent smeared area
C_1	relaxation coefficient for normal stress components
C_2	relaxation coefficient for shear stress components
c'	soil cohesion
c_k	stiffness proportional, Rayleigh damping coefficient
c_m	mass proportional, Rayleigh damping coefficient
c_r	cohesion due to reinforcement
d_{eq}	thickness of the plate
E	Young's modulus

E_{Al}	Young's modulus the Aluminium
E_{rubber}	Young's modulus of the rubber
e	void ratio
e_{init}	initial void ratio
e_{crit}	critical void ratio
e_{max}	maximum void ratio
e_{min}	minimum void ratio
E_{50}^{ref}	triaxial secant stiffness (at 50% of deviatoric failure stress in drained triaxial compression
E_{oed}^{ref}	oedometric tangent stiffness (in compression)
E_{ur}^{ref}	unloading-reloading stiffness
f_{lower}	lower frequency
f_{upper}	upper frequency
f_0	natural frequency
G	secant shear modulus
G_{rubber}	shear modulus of rubber layer
G_r	shear modulus of rooted soil
G_s	shear modulus of fallow soil
G_0	maximum shear modulus
G_0^{ref}	small strain modulus
$\boldsymbol{g}$	acceleration due to gravity(=9.81m/s^2)
I	second moment of area
I_D	relative density
K_0	Lateral earth pressure coefficient
m'	power –law index for stress-level
M_s	surface wave magnitude
p	reaction from soil due to the deflection of pile
r	radius
R_f	ratio of deviatoric failure stress to asymptotic limiting deviator stress
S	spacing of roots
S_{fallow}	crest settlement of fallow slope
S_{rooted}	crest settlement of rooted slope
v	velocity
V_P	pressure wave velocity

V_s	shear wave velocity
w	unit weight of plate
w_{Al}	weight of the aluminium frame plate
y	deflection
α	Newmark time integration coefficient
β	Newmark time integration coefficient
$\varepsilon_{s,0.7}$	shear strain
γ	unit weight
γ_r	threshold shear strain
γ	soil unit weight
ψ'	effective angle of dilation
θ	slope angle
u	displacement
ν	Poisson's ratio
ν_{rubber}	Poisson's ratio of rubber
ν_{Al}	Poisson's ratio of Aluminium
ν_{ur}	Poisson's ratio(unload-reload)
ρ	density of the soil
Δ	difference on damping ratio
σ_n	normal stress
σ_v	vertical confining stress
ϕ'	effective angle of friction
ϕ'_{crit}	critical angle of friction
ϕ'_{eq}	equivalent angle of friction
ϕ'_{pk}	(secant) peak angle of friction
τ	shear stress
ζ_{add}	additional Rayleigh damping ratio
$\zeta_{desired}$	target additional Rayleigh damping ratio
$\zeta_{\max}$	maximum additional Rayleigh damping ratio
$\zeta_{\min}$	minimum additional Rayleigh damping ratio
ζ_r	additional Rayleigh damping ratio of rooted soil
ζ_s	additional Rayleigh damping ratio of fallow soil

References

Al-Defae, A.H., Caucis, K., and Knappett, J.A. (2013). Aftershocks and the whole-life seismic performance of granular slopes. *Géotechnique* 63, No. 14, 1230–1244, 10.1680/geot.12.P.149.

Amorosi, A., Boldini, D., and Elia, G. (2010). Parametric study on seismic ground response by finite element modelling. *Computers and Geotechnics* 37, No. 4, 515–528, Elsevier Ltd. 10.1016/j.compgeo.2010.02.005.

Bathe, K.J., and Saunders, H. (1984). Finite Element Procedures in Engineering Analysis., 10.1115/1.3264375.

Bertalot, D. (2013). Foundations on layered liquefiable soils., PhD thesis,University of Dundee,UK.

Blatz, J.A., Ferreira, N.J., and Graham, J. (2004). Effects of near-surface environmental conditions on instability of an unsaturated soil slope. *Canadian Geotechnical Journal* 41, No. 6, 1111–1126, 10.1139/t04-058.

Boldrin, D., Leung, A.K., and Bengough, A.G. (2017). Correlating hydrologic reinforcement of vegetated soil with plant traits during establishment of woody perennials. *Plant and Soil* 1–15, 10.1007/s11104-017-3211-3.

Bolton, M.D., and Take, W.A. (2011). Seasonal ratcheting and softening in clay slopes, leading to first-time failure. *Géotechnique* 61, No. 9, 757–769, 10.1680/geot.9.P.125.

Bourrier, F., Kneib, F., Chareyre, B., and Fourcaud, T. (2013). Discrete modeling of granular soils reinforcement by plant roots. *Ecological Engineering* 61, No. 1 PARTC, 646–657, 10.1016/j.ecoleng.2013.05.002.

Brennan, A.J., Thusyanthan, N.I., and Madabhushi, S.P.G. (2005). Evaluation of shear modulus and damping in dynamic centrifuge tests. *Journal of Geotechnical and Geoenvironmental Engineering* 131, No. 12, 1488–1497, 10.1061/(ASCE)1090-0241(2005)131:12(1488).

BSI (2007). BS EN 1999-1-1:2007 - Eurocode 9: Design of aluminium structures - Part 1-1: General Structural rules.

Canadell, J., Jackson, R.B., Ehleringer, J.B., Mooney, H. a., Sala, O.E., and Schulze, E.-D. (1996). Maximum rooting depth of vegetation types at the global scale. *Oecologia* 108, No. 4, 583–595, 10.1007/BF00329030.

Chen, T., Fang, Y., and Asce, M. (2008). Earth Pressure due to Vibratory Compaction. *Journal of Geotechnical and Geoenvironmental Engineering* 134, No. 4, 437–444.

Coop, M.R., and Atkinson, J.H. (1993). The mechanics of cemented carbonate sands. *Géotechnique* 43, No. 1, 53–67, 10.1680/geot.1993.43.1.53.

Duncan, J.M., and Seed, R. (1986). Compaction-induced earth pressures under Ko-conditions. *Journal of Geotechnical Engineering* 112, No. 1, 1–12.

Elia, G., Amorosi, A., Chan, A.H.C., and Kavvadas, M.J. (2011). Fully coupled dynamic analysis of an earth dam. *Géotechnique* 61, No. 7, 549–563, 10.1680/geot.8.P.028.

Frydman, S., and Operstein, V. (2001). Numerical simulation of direct shear of rootreinforced soil. *Proceedings of the ICE - Ground Improvement* 5, No. 1, 41–48, 10.1680/grim.2001.5.1.41.

Gilman, E.F. (1989). Prediction root spread from trunk diameter and branch spread. *Arboricultural Journal* 13, No. 1, 25–32, 10.1080/03071375.1989.9756398.

Göttlicher, S.G., Taylor, A.F.S., Grip, H., Betson, N.R., Valinger, E., Högberg, M.N., and Högberg, P. (2008). The lateral spread of tree root systems in boreal forests: Estimates based on 15N uptake and distribution of sporocarps of ectomycorrhizal fungi. *Forest Ecology and Management* 255, No. 1, 75–81, 10.1016/j.foreco.2007.08.032.

Griffiths, D.V., and Lane, P. a. (1999). Slope stability analysis by finite elements. *Géotechnique* 49, No. 3, 387–403, 10.1680/geot.1999.49.3.387.

Hall, J.F. (2006). Problems encountered from the use (or misuse) of Rayleigh damping. *Earthquake Engineering and Structural Dynamics* 35, No. 5, 525–545, 10.1002/eqe.541.

Highways Agency. (2016). Manual of contract documents for highway works Volume 1 Specification for highway works.

Ingold, T.S. (1979). The effects of compaction. *Géotechnique* 29, No. 3, 265–283.

Jackson, R.B., Canadell, J., Ehleringer, J.R., Mooney, H. a., Sala, O.E., and Schulze, E.D. (1996). A global analysis of root distributions for terrestrial biomes. *Oecologia* 108, No. 3, 389–411, 10.1007/BF00333714.

Jarvis, N.J. (2011). Simple physics-based models of compensatory plant water uptake: Concepts and eco-hydrological consequences. *Hydrology and Earth System Sciences* 15, No. 11, 3431–3446, 10.5194/hess-15-3431-2011.

Kellezi, L. (2000). Local transmitting boundaries for transient elastic analysis. *Soil Dynamics and Earthquake Engineering* 19, No. 7, 533–547, 10.1016/S0267-7261(00)00029-4.

Knappett, J.A., Madden, P., and Caucis, K. (2015). Seismic structure–soil–structure interaction between pairs of adjacent building structures. *Géotechnique* 65, No. 5, 429–441, 10.1680/geot.SIP.14.P.059.

Kontoe, S., Zdravkovic, L., and Potts, D.M. (2009). An assessment of the domain reduction method as an advanced boundary condition and some pitfalls in the use of conventional absorbing boundaries. *International Journal for Numerical and Analytical Methods in Geomechanics* 33, No. 3, 309–330, 10.1002/nag.713.

Lauder, K. (2010). The performance of pipeline ploughs., PhD thesis,University of Dundee,UK.

Leung, A.K., Boldrin, D., Liang, T., Wu, Z.Y., Kamchoom, V., and Bengough, A.G. (2018). Plant age effects on soil infiltration rate during early plant establishment. Géotechnique 68, No. 7, 646–652, 10.1680/jgeot.17.t.037.

Leung, A.K., and Ng, C.W.W. (2013). Analyses of groundwater flow and plant evapotranspiration in a vegetated soil slope. *Canadian Geotechnical Journal* 50, No. 12, 1204–1218, 10.1139/cgj-2013-0148.

Liang, T., Bengough, A.G., Knappett, J.A., MuirWood, D., Loades, K.W., Hallett, P.D., Boldrin, D., Leung, A.K., and Meijer, G.J. (2017a). Scaling of the reinforcement of soil slopes by living plants in a geotechnical centrifuge. *Ecological Engineering* 109, No. Part B, 207–227, 10.1016/j.ecoleng.2017.06.067.

Liang, T., and Knappett, J.A. (2017a). Newmark sliding block model for predicting the seismic performance of vegetated slopes. *Soil Dynamics and Earthquake Engineering* 101 27–40, 10.1016/j.soildyn.2017.07.010.

Liang, T., and Knappett, J.A. (2017b). Centrifuge modelling of the influence of slope height on the seismic performance of rooted slopes. *Géotechnique* 67, No. 10, 855–869, 10.1680/jgeot.16.P.072.

Liang, T., Knappett, J.A., and Duckett, N. (2015). Modelling the seismic performance of rooted slopes from individual root–soil interaction to global slope behaviour. *Géotechnique* 65, No. 12, 995–1009, 10.1680/jgeot.14.P.207.

Lin, D.G., Huang, B.S., and Lin, S.H. (2010). 3-D numerical investigations into the shear strength of the soil-root system of Makino bamboo and its effect on slope stability. *Ecological Engineering* 36, No. 8, 992–1006, 10.1016/j.ecoleng.2010.04.005.

Lysmer, J., and Kuhlemeyer, R.L. (1969). Finite Dynamic Model For Infinite Media. *Journal of the Engineering Mechanics Division* 95, No. 4, 859–878.

Mao, Z., Bourrier, F., Stokes, A., and Fourcaud, T. (2014a). Three-dimensional modelling of slope stability in heterogeneous montane forest ecosystems. *Ecological Modelling* 273 11–22, Elsevier B.V. 10.1016/j.ecolmodel.2013.10.017.

Mao, Z., Yang, M., Bourrier, F., and Fourcaud, T. (2014b). Evaluation of root reinforcement models using numerical modelling approaches. *Plant and Soil* 381, No. 1–2, 249–270, 10.1007/s11104-014-2116-7.

Meijer, G.J., Bengough, A.G., Knappett, J.A., Loades, K.W. & Nicoll, B.C. (2016). An evaluation of new in-situ techniques for measuring the properties of root reinforced soil. *Géotechnique*, 66, No. 1: 27-40, 10.1680/jgeot.15.P.060.

Meijer, G.J., Bengough, A.G., Knappett, J.A., Loades, K.W. & Nicoll, B.C. (2018). In-situ measurement of root-reinforcement using the corkscrew extraction method. *Canadian Geotechnical J*ournal, 55, No. 10: 1372-1390, 10.1139/cgj-2017-0344.

Mooney, M.A., and Rinehart, R. V (2009). In Situ Soil Response to Vibratory Loading and Its Relationship to Roller-Measured Soil Stiffness. *Journal of Geotechnical and Geoenvironmental Engineering* 135, No. 8, 1022–1031, 10.1061/(ASCE)GT.1943-5606.0000046.

Ng, C.W.W., Kamchoom, V., and Leung, A.K. (2016). Centrifuge modelling of the effects of root geometry on transpiration-induced suction and stability of vegetated slopes. *Landslides* 13, No. 5, 925–938, 10.1007/s10346-015-0645-7.

Norris, J.E., Stokes, A., Mickovski, S.B., Cammeraat, E., Van Beek, R., Nicoll, B.C., and Achim, A. (2008). Slope stability and erosion control: Ecotechnological solutions., Springer, Netherlands. 10.1007/978-1-4020-6676-4.

Nyambayo, V.P., and Potts, D.M. (2010). Numerical simulation of evapotranspiration using a root water uptake model. *Computers and Geotechnics* 37, No. 1–2, 175–186, Elsevier Ltd. 10.1016/j.compgeo.2009.08.008.

Pelecanos, L., Kontoe, S., and Zdravković, L. (2013). Numerical modelling of hydrodynamic pressures on dams. *Computers and Geotechnics* 53 68–82, 10.1016/j.compgeo.2013.04.003.

Pelecanos, L., Kontoe, S., and Zdravković, L. (2015). A case study on the seismic performance of earth dams. *Géotechnique* 65, No. 11, 923–935, 10.1680/jgeot.SIP.15.P.009.

Pollen, N., and Simon, A. (2005). Estimating the mechanical effects of riparian vegetation on stream bank stability using a fiber bundle model. *Water Resources Research* 41, No. 7, 1–11, 10.1029/2004WR003801.

Potts, D.M., Dounias, G.T., and Vaughan, P.R. (1990). Finite element analysis of progressive failure of Carsington embankment. *Geotechnique* 40, No. 1, 79–101, 10.1680/geot.1990.40.1.79.

Potts, D.M., Kovacevic, N., and Vaughan, P.R. (1997). Delayed collapse of cut slopes in stiff clay. *Géotechnique* 47, No. 5, 953–982, 10.1680/geot.1997.47.5.953.

Preti, F. (2013). Forest protection and protection forest: Tree root degradation over hydrological shallow landslides triggering. *Ecological Engineering* 61, No. Part C, 633–645, http://dx.doi.org/10.1016/j.ecoleng.2012.11.009.

Prevost, B.J.H., Asce, M., Abdel-ghaffar, A.M., and Lacy, S.J. (1985). Nonlinear Dynamic Analyses of an Earth Dam. *Journal of Geotechnical Engineering* 111, No. 7, 882–897, 10.1061/(ASCE)0733-9410(1985)111:7(882).

Reese, L.C., and Van Impe, W.F. (2011). Single Piles and Pile Groups Under Lateral Loading (2nd Edition). *CRC Press* 508, 10.1115/1.1445326.

Roy, D., and Campanella, R.G. (1996). Angles of friction and dilatancy of sand. *Géotechnique* 46, No. 1, 145–151, 10.1680/geot.1997.47.4.887.

Dos Santos, J.A., and Correia, A.G. (2001). Reference threshold shear strain of soil. Its application to obtain an unique strain-dependent shear modulus curve for soil. *In* Proceedings of the 15th international conference on soil mechanics and geotechnical engineering, Istanbul, Turkey. pp. 267–270.

Schanz, T., Vermeer, A., and Bonnier, P. (1999). The hardening soil model: formulation and verification. *In* Beyond 2000 in computational geotechnics: Ten Years of PLAXIS International. *Edited by* Ronald B.J. Brinkgreve, CRC Press; 1 edition (1 Jan. 1999). pp. 281–296.

Schenk, H.J., and Jackson, R.B. (2002). Rooting depths, lateral root spreads and below-ground/above-ground allometries of plants in water-limited ecosystems. *Journal of Ecology* 90, No. 3, 480–494, 10.1046/j.1365-2745.2002.00682.x.

Schmidt, K.M., Roering, J.J., Stock, J.D., Dietrich, W.E., Montgomery, D.R., and Schaub, T. (2001). The variability of root cohesion as an influence on coast range. *Canadian Geotechnical Journal* 38, No. 5, 995–1024, 10.1139/cgj-38-5-995.

Schwarz, M., Lehmann, P., and Or, D. (2010). Quantifying lateral root reinforcement in steep slopes - from a bundle of roots to tree stands. *Earth Surface Processes and Landforms* 35, No. 3, 354–367, 10.1002/esp.1927.

Sidle, R.C., and Bogaard, T.A. (2016). Dynamic earth system and ecological controls of rainfall-initiated landslides. Earth-Science Reviews 159, 275–291, 10.1016/j.earscirev.2016.05.013.

Simon, A., and Collison, A.J.C. (2002). Quantifying the mechanical and hydrologic effects of riparian vegetation on streambank stability. *Earth Surface Processes and Landforms* 27, No. 5, 527–546, 10.1002/esp.325.

Skempton, A.W. (1996). Embankments and Cuttings on the early Railways. *Construction History* 11 33–49.

Smethurst, J., Clarke, D., and Powrie, W. (2006). Seasonal changes in pore water pressure in a grass covered cut slope in London clay. *Geotechnique* 56, No. 8, 523–537, 10.1680/geot.2006.56.8.523.

Smethurst, J., Clarke, D., and Powrie, W. (2012). Factors controlling the seasonal variation in soil water content and pore water pressures within a lightly vegetated clay slope. *Geotechnique* 62, No. 5, 429–446.

Stokes, A., Atger, C., Bengough, A.G., Fourcaud, T., and Sidle, R.C. (2009). Desirable Plant root traits for protecting natural and engineered slopes against landslides. *Plant and Soil* 324, No. 1, 1–30, 10.1007/s11104-009-0159-y.

Stokes, A., Douglas, G.B., Fourcaud, T., Giadrossich, F., Gillies, C., Hubble, T., Kim, J.H., Loades, K.W., Mao, Z., McIvor, I.R., Mickovski, S.B., Mitchell, S., Osman, N., Phillips, C., Poesen, J., Polster, D., Preti, F., Raymond, P., Rey, F., Schwarz, M., and Walker, L.R. (2014). Ecological mitigation of hillslope instability: Ten key issues facing researchers and practitioners. *Plant and Soil* 377, No. 1–2, 1–23, 10.1007/s11104-014-2044-6.

Temgoua, A.G.T., Kokutse, N.K., and Kavazoovic´, Z. (2016). Influence of forest stands and root morphologies on hillslope stability. *Ecological Engineering* 95 622–634, 10.1016/j.ecoleng.2016.06.073.

Tsiampousi, A., Zdravkovic, L., and Potts, D.M. (2017). Numerical Study of the Effect of Soil – Atmosphere Interaction on the Stability and Serviceability of Cut Slopes in London Clay. *Canadian Geotechnical Journal* 54, No. October 2016, 405–418, 10.1139/cgj-2016-0319.

Vergani, C., Chiaradia, E.A., Bassanelli, C., and Bischetti, G.B. (2014). Root strength and density decay after felling in a Silver Fir-Norway Spruce stand in the Italian Alps. *Plant and Soil* 377, No. 1–2, 63–81, 10.1007/s11104-013-1860-4.

Veylon, G., Ghestem, M., Stokes, A., and Bernard, A. (2015). Quantification of mechanical and hydric components of soil reinforcement by plant roots. Canadian Geotechnical Journal 52, No. 11, 1839–1849, 10.1139/cgj-2014-0090.

Vince, A., and Askenazi, A. (1999). Building better products with finite element analysis., Vol. 1. Singapore: OnWord Press.

Wood, D.M., Diambra, A., and Ibraim, E. (2016). Fibres and soils : a route towards modelling of root-soil systems. *Soils and Foundations* 56, No. 5, 765–778, 10.1016/j.sandf.2016.08.003.

Woodward, P.K., and Griffiths, D. V. (1996). Influence of Viscous Damping in the Dynamic Analysis of an Earth Dam Using Simple Constitutive Models. *Computers and Geotechnics* 19, No. 3, 245–263, 10.1016/0266-352X(96)00002-X.

Wu, T.H. (1976). Investigation of Landslides on Prince of Wales Island, Alaska. *Geotechnical Engineering Report 5. Civil Engineering Department, Ohio State University, Columbus, Ohio, USA* .

Wu, T.H. (2013). Root reinforcement of soil: review of analytical models, test results, and applications to design. *Canadian Geotechnical Journal* 50, No. 3, 259–274.

Zeng, X., and Schofield, A.N. (1996). Design and performance of an equivalent-shear-beam container for earthquake centrifuge modelling. *Géotechnique* 46, No. 1, 83–102, 10.1680/geot.1996.46.1.83.

Table 1. Summary of centrifuge models tested

Test identification number	**Test scale**	**Slope height (m)**	**Root type**	**Plant spacing (m)**	**Motion frequency content (Hz)**	**Soil relative density, I_D (%)**
TL 04	1:10 (10-g)	2.4	Fallow	N/A	4-30	57
TL 05	1:30 (30-g)	7.2	Fallow	N/A	1.33-10	55
TL 06	1:30 (30-g)	7.2	1:30 root cluster	1.4 × 2.4	1.33-10	60
TL 07	1:10 (10-g)	2.4	1:10 root cluster	1.4 × 2.4	4-30	60
TL 08	1:30 (30-g)	7.2	Fallow	N/A	4-10	57
TL 09	1:30 (30-g)	7.2	1:30 root cluster	1.4 × 2.4	4-10	59

Accepted manuscript doi:
10.1680/jgeot.17.p.128

Table 2. Key parameters and properties of ESB container wall elements

	Parameter	Units	Bottom rubber layer	2nd rubber layer	3rd rubber layer	4th rubber layer	Top rubber layer	Aluminium frame
1:10 scale model	*EA*	kN/m	2268	2124	1979	1835	1690	25.88×10^6
	EI	kN m^2/m	26.58	24.89	23.19	21.50	19.81	0.303×10^6
	GA	kN/m	630	590	549.7222	509.7222	469.4	8.08×10^6
1:30 scale model	*EA*	kN/m	11130	9838	8538	7237	5937	77.63×10^6
	EI	kN m^2/m	1175	1038	900.5	763.3	626.2	8.187×10^6
	GA	kN/m	3092	2733	2372	2010	1649	24.25×10^6

Table 3. Key parameters and properties of ESB container wall elements

Parameter	Units	1:10 scale model		1:30 scale model	
		Rubber layer	Aluminium frame	Rubber layer	Aluminium frame
w	kN /m/m	0	19.23	0	57.69
v	-	0.5	0.334	0.5	0.334
ζ_{add}	%	5	0.04	5	0.04
c_m	-	2.698	0.0216	0.8975	7.180×10^{-3}
c_k	-	0.5695×10^{-3}	4.559×10^{-6}	1.709×10^{-3}	0.01368×10^{-3}

Table 4. Constitutive parameters for HST95 sand (after Al-Defae *et al*. 2013)

Parameter	Al-Defae et al. (2013)	Units
γ	$3I_D$+14.5	kN/m^3
E_{50}^{ref}	$1.25E_{oed}^{ref}$	MPa
E_{oed}^{ref}	$25I_D$+20.22	MPa
E_{ur}^{ref}	$3E_{oed}^{ref}$	MPa
v_{ur}	0.2	-
G_0^{ref}	$50I_D$+88.80	MPa
m'	0.6-0.1I_D	-
$\varepsilon_{s,0.7}$	$1.7I_D$+0.67($\times 10^{-4}$)	-
R_f	0.9	-
c'	0.3	kPa

Accepted manuscript doi:
10.1680/jgeot.17.p.128

Table 5. Calibrated additional Rayleigh damping parameters for soil

Model ID	Additional equivalent viscous damping ratio	Motion frequency content (Hz)	Maximum additional viscous damping ratio ζ_{max} (see Fig. 6)	c_m	c_k
TL 04	1.5%	4-30	1.83%	0.8116	0.1713×10^{-3}
TL 05	3%	1.33-10	3.65%	0.5384	1.025×10^{-3}
TL 06	3%	1.33-10	3.65%	0.5384	1.025×10^{-3}
TL07	1.5%	4-30	1.83%	0.8116	0.1713×10^{-3}
TL 08	2.5%	4-10	2.63%	0.9443	0.5980×10^{-3}
TL 09	2.5%	4-10	2.63%	0.9443	0.5980×10^{-3}

Figure captions

Fig. 1 Finite Element mesh for semi-infinite lateral boundary conditions for 1:30 scale model: (a) centrifuge case; (b) compacted embankment case; (c) end-tipped embankment case (d) cutting case.

Fig. 2 Finite Element mesh of ESB container boundary model.

Fig. 3 Input motions in the time domain.

Fig. 4 Apparent root cohesion for 1:10 and 1:30 scale root cluster: (a) variation of confining stress; (b) measured and input root 'cohesion'. Depths shown at prototype scale.

Fig. 5 Modelling of additional Rayleigh damping in the Finite Element simulations.

Fig. 6 Effect of additional damping on measured and predicted crest accelerations in the frequency domain.

Fig. 7 Comparison of Finite Element and centrifuge permanent crest settlement for different input soil strength parameters: (a) 1:30 scale fallow slope at full frequency content; (b) 1:30 scale model at reduced frequency content.

Fig. 8 Comparison of Finite Element and centrifuge shear stress-strain loops at midpoint of 1:30 scale fallow slopes at full frequency during EQ2.

Fig. 9 Comparison of Finite Element and centrifuge permanent crest settlement for rooted and fallow models: (a) 1:30 scale model at full frequency content; (b) 1:30 scale model at reduced frequency content.

Fig. 10 Comparison of seismic slope performance (at slope crest) between semi-infinite lateral soil boundaries and ESB container boundaries for 1:30 scale fallow slope: (a) acceleration; (b) permanent settlement.

Fig. 11 Input additional Rayleigh damping ratio for parametric study.

Fig. 12 Influence of rooted soil zone parameters on permanent deformation response at the crest: (a) root cohesion; (b) rooted zone damping; (c) rooted zone stiffness; (d) width of rooted zone.

Fig. 13 Influence of rooted soil zone parameters on peak ground acceleration (PGA) response at the crest: (a) root cohesion; (b) rooted zone damping; (c) rooted zone stiffness; (d) width of rooted zone.

Fig. 14 Comparison of pre-earthquake stress-strain state (in terms of vertical and horizontal effective stress) in a 4.8 m high slope: (a) centrifuge case; (b) compacted embankment case; (c) end-tipped embankment case; (d) cutting case.

Fig. 15 Distribution of horizontal stress with depth at different positions within a 4.8 m high slope: (a) beneath slope crest; (b) middle of the slope surface.

Fig. 16 Influence of construction technique on seismic performance of vegetated slopes: (a) permanent deformation response at the crest; (b) peak ground acceleration (PGA) response at the crest.

Fig. 17 Influence of apparent soil cohesion and slope angle on the effectiveness of roots as a performance-improving remedial technique for cutting case: (a) static factor of safety (FOS); (b) permanent deformation response; (c) PGA response.

Accepted manuscript doi:
10.1680/jgeot.17.p.128

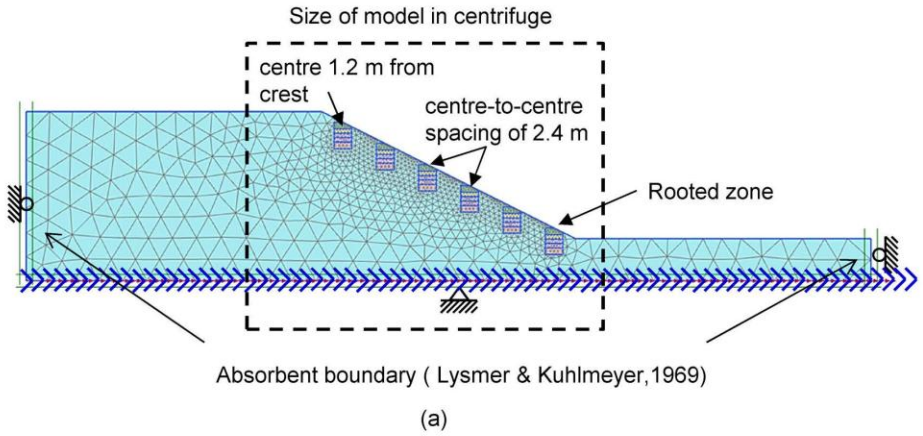

KnappettFig1.tif

Accepted manuscript doi:
10.1680/jgeot.17.p.128

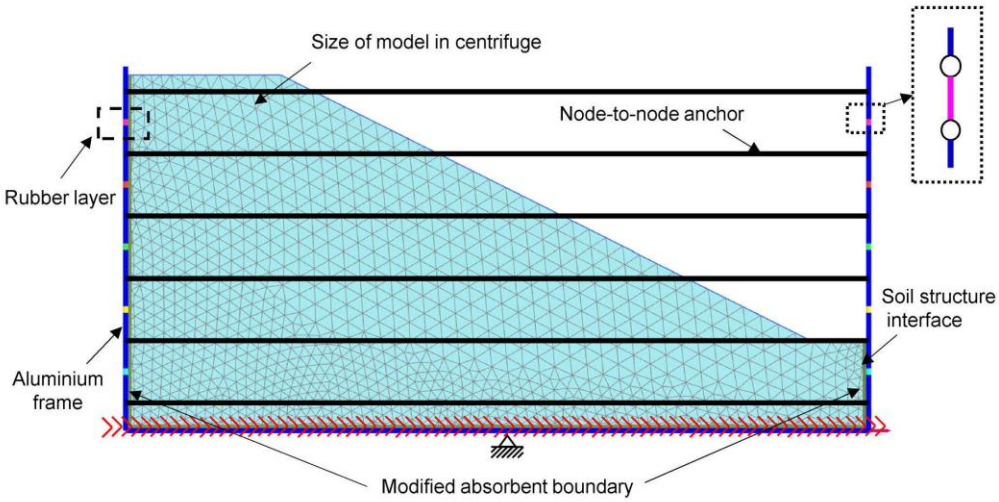

KnappettFig2.tif

Accepted manuscript doi:
10.1680/jgeot.17.p.128

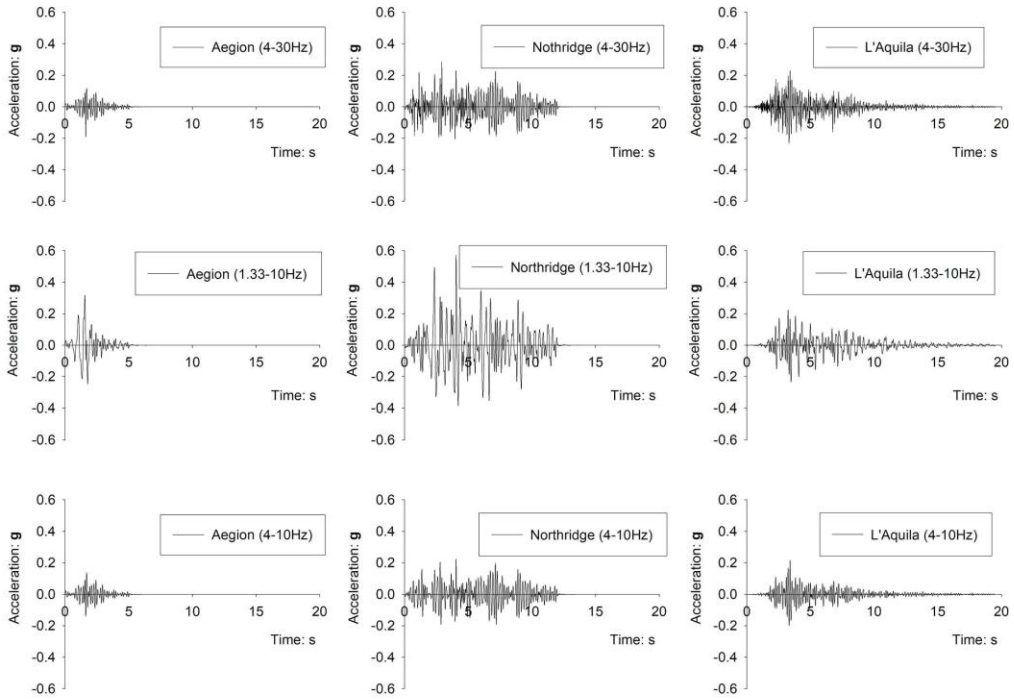

KnappettFig3.tif

Accepted manuscript doi:
10.1680/jgeot.17.p.128

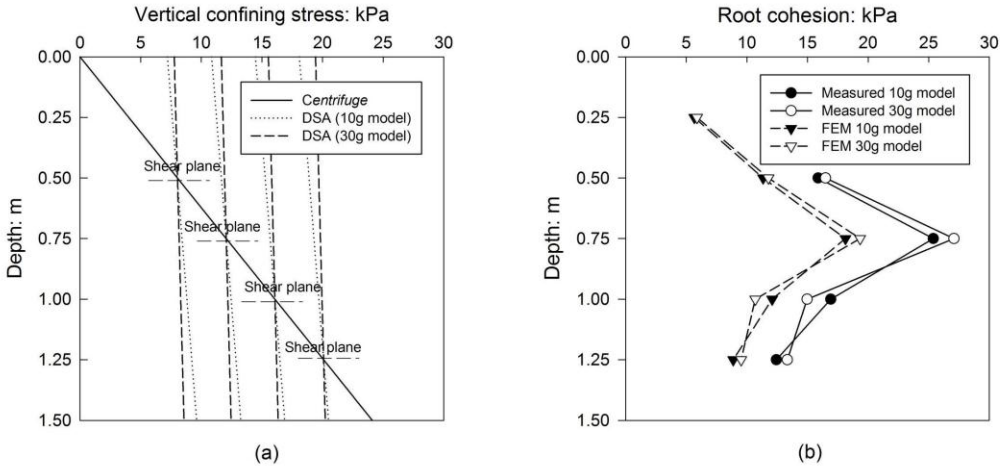

KnappettFig4.tif

Accepted manuscript doi:
10.1680/jgeot.17.p.128

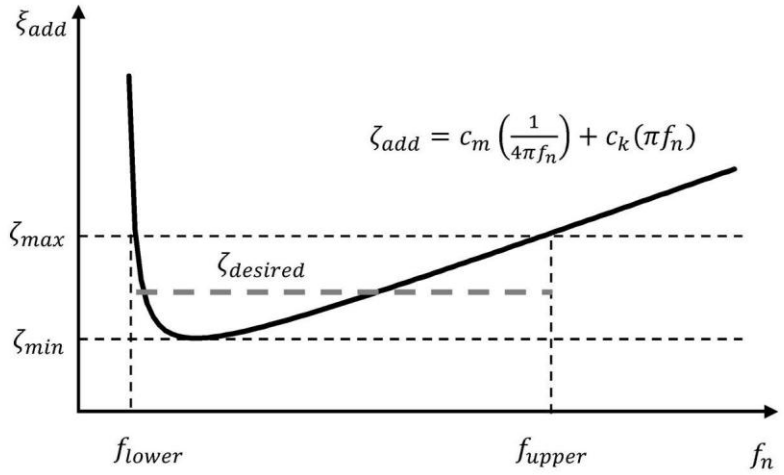

KnappettFig5.tif

Accepted manuscript doi:
10.1680/jgeot.17.p.128

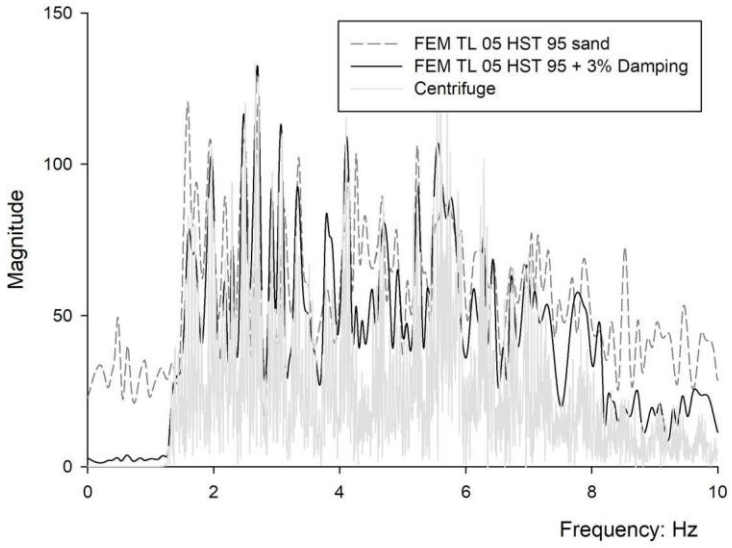

KnappettFig6.tif

Accepted manuscript doi:
10.1680/jgeot.17.p.128

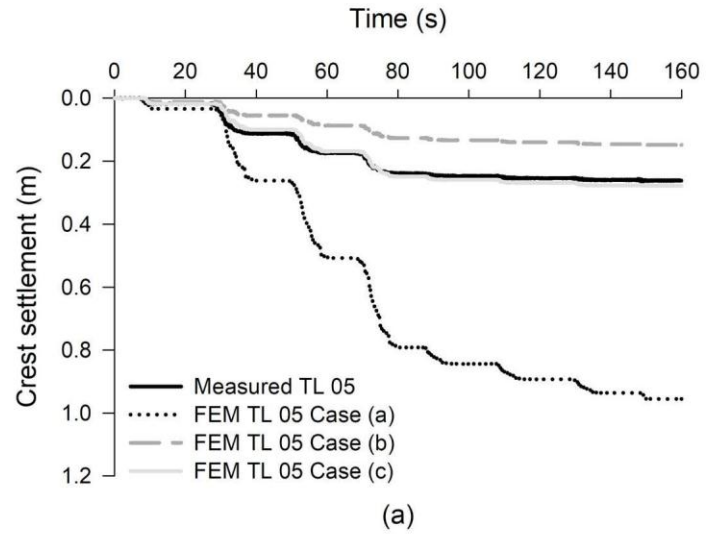

(a)

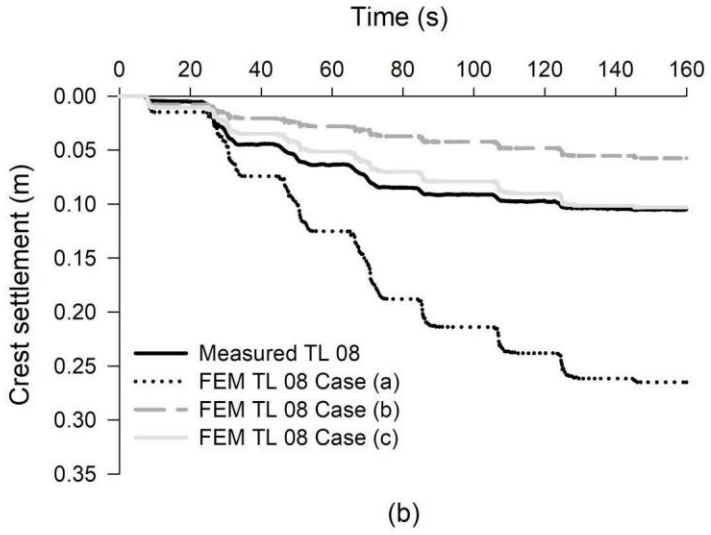

(b)

KnappettFig7.tif

Accepted manuscript doi:
10.1680/jgeot.17.p.128

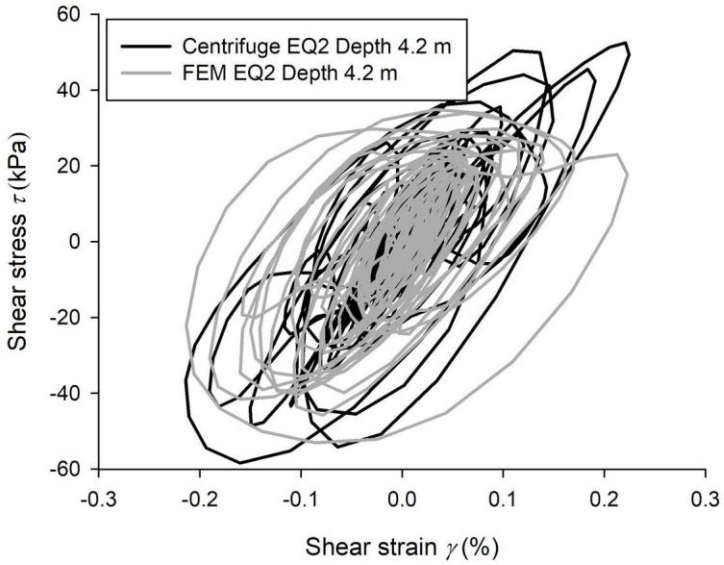

KnappettFig8.tif

Accepted manuscript doi:
10.1680/jgeot.17.p.128

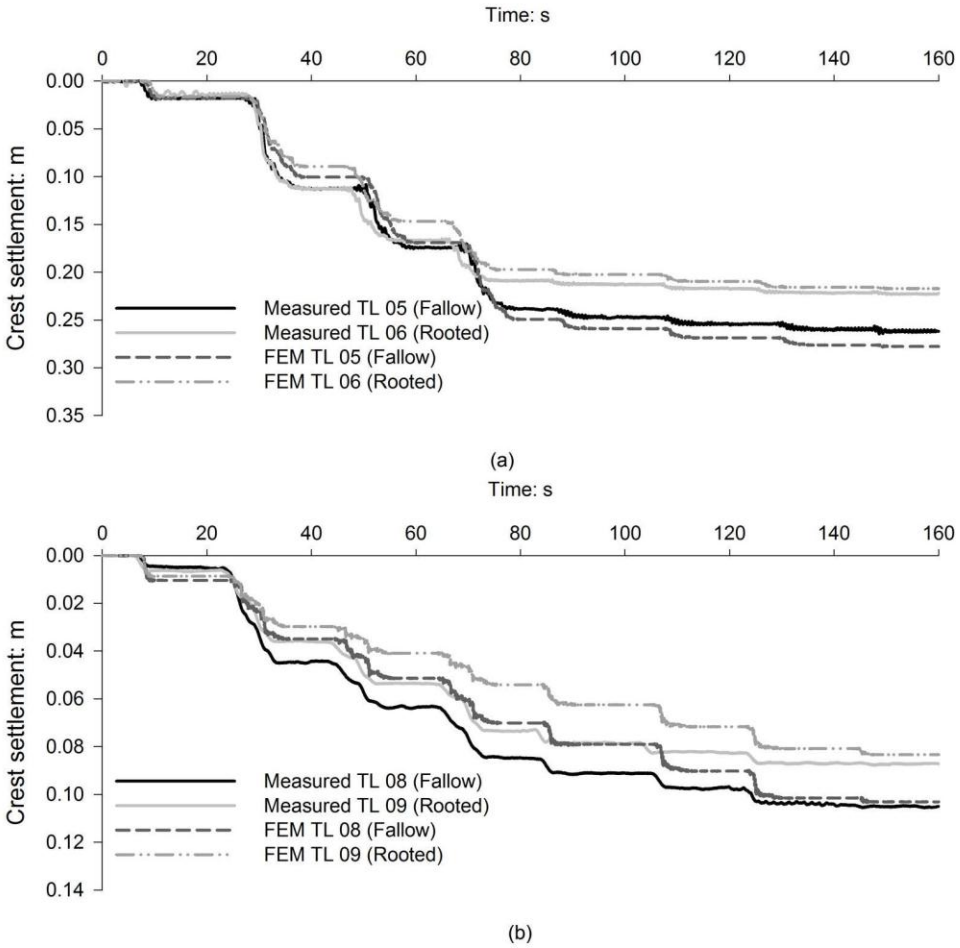

KnappettFig9.tif

Accepted manuscript doi:
10.1680/jgeot.17.p.128

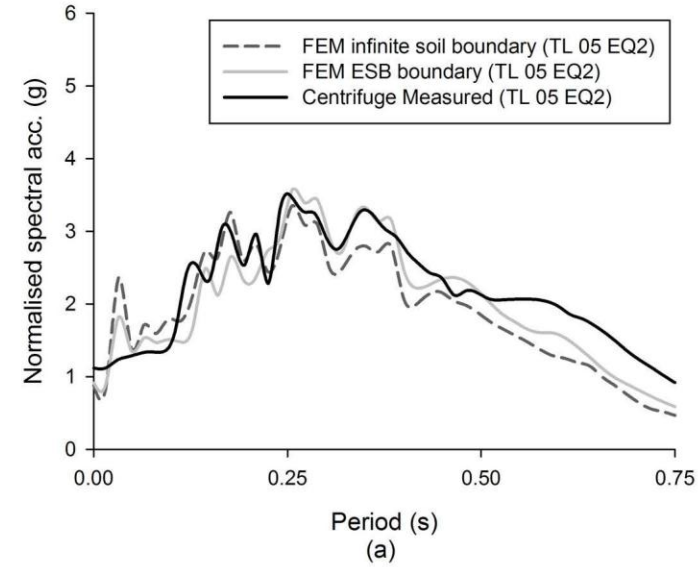

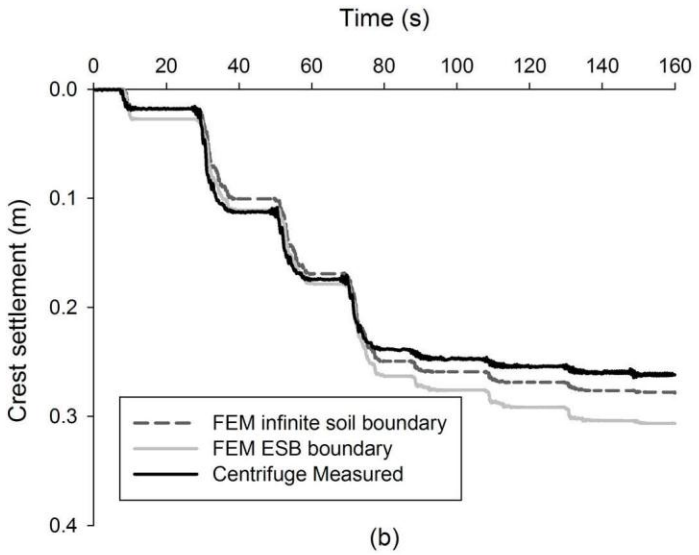

KnappettFig10.tif

Accepted manuscript doi:
10.1680/jgeot.17.p.128

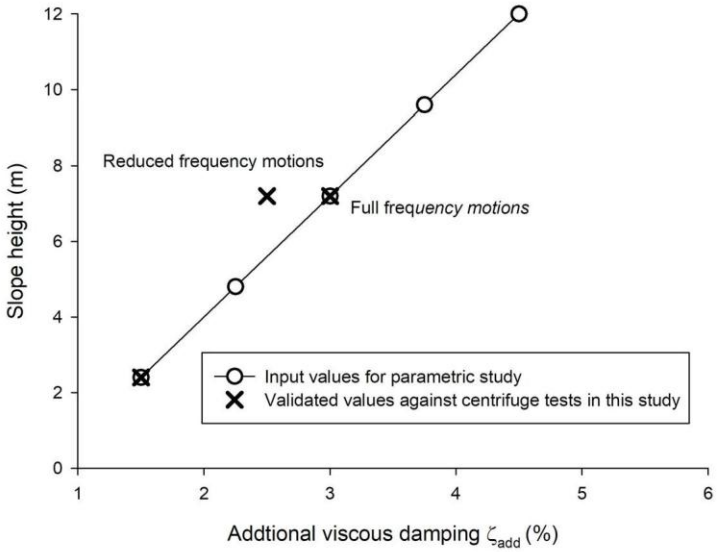

KnappettFig11.tif

Accepted manuscript doi:
10.1680/jgeot.17.p.128

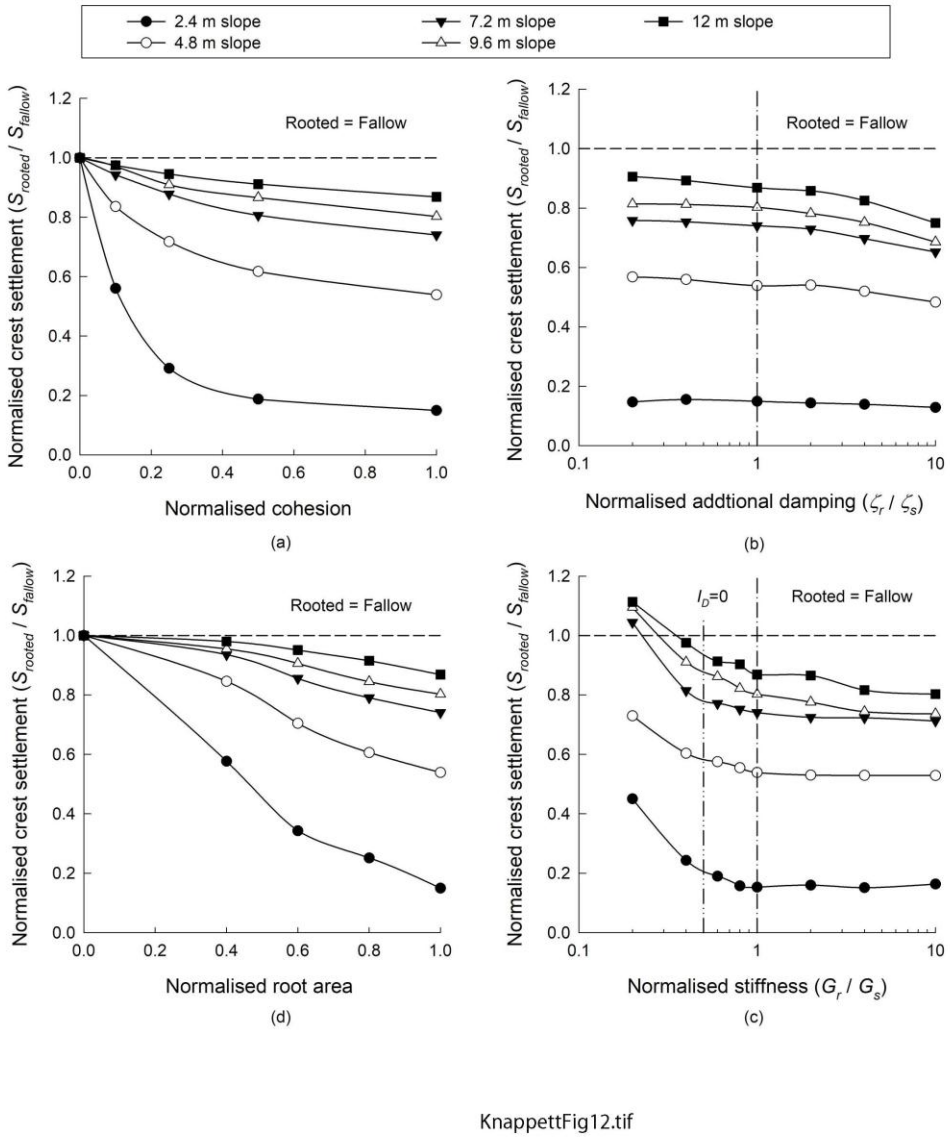

KnappettFig12.tif

Accepted manuscript doi:
10.1680/jgeot.17.p.128

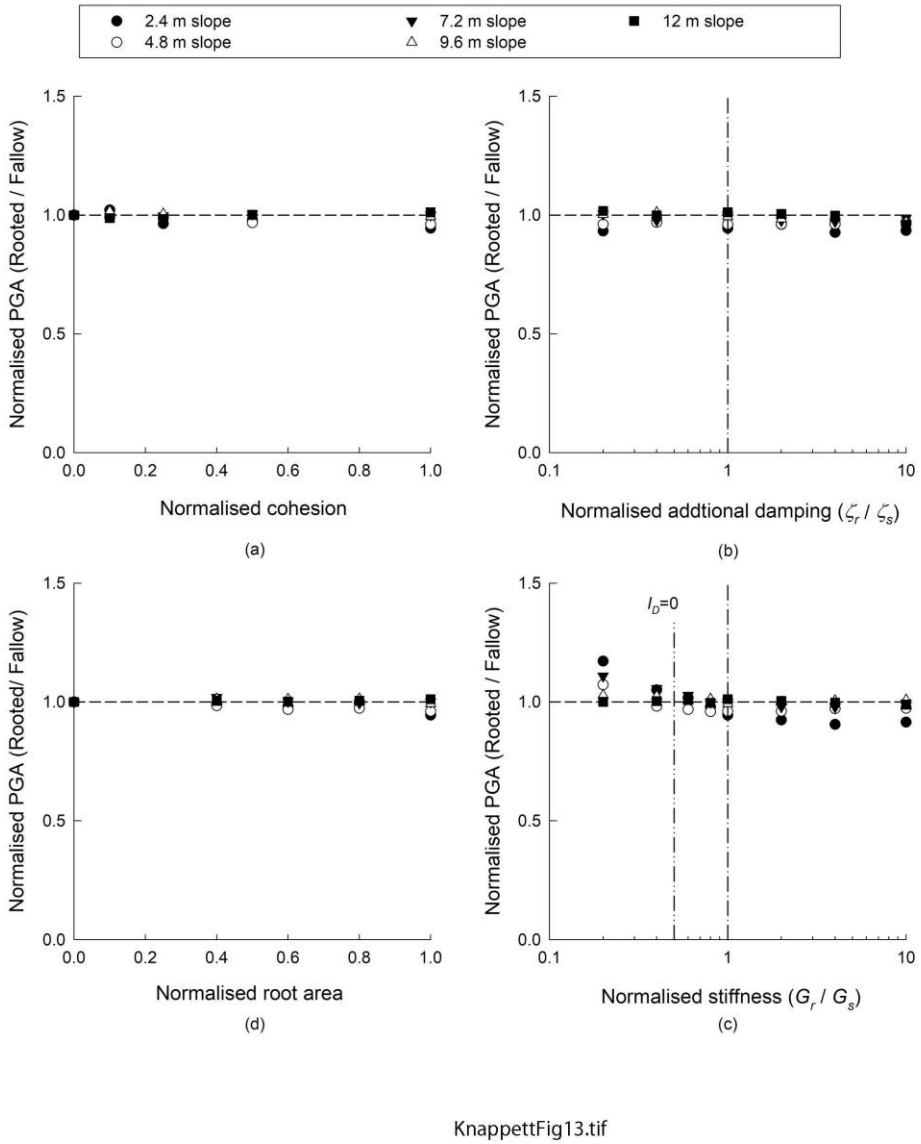

KnappettFig13.tif

Accepted manuscript doi:
10.1680/jgeot.17.p.128

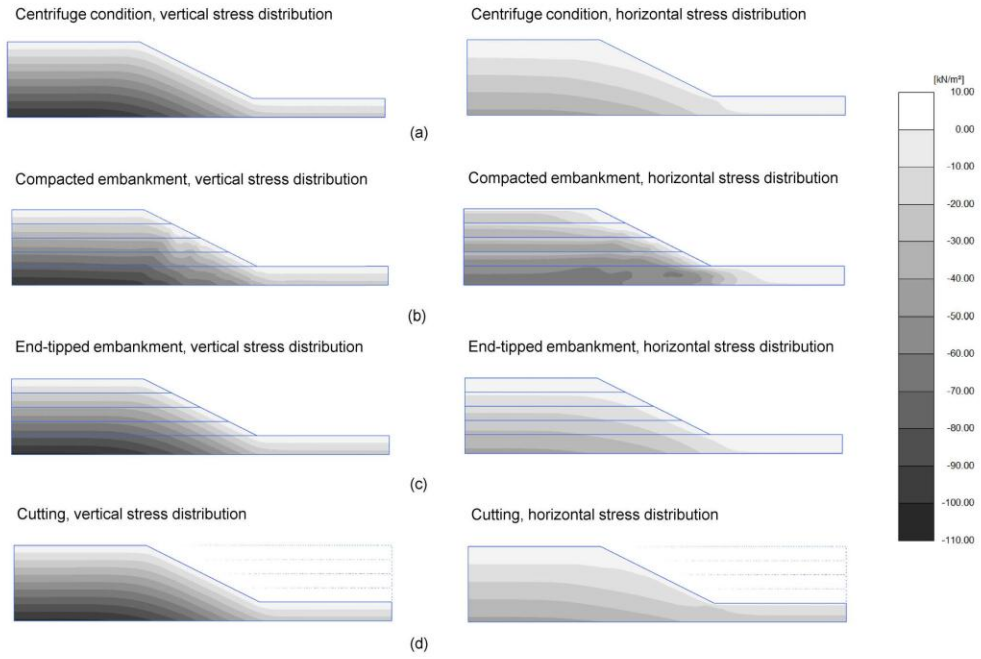

KnappettFig14.tif

Accepted manuscript doi:
10.1680/jgeot.17.p.128

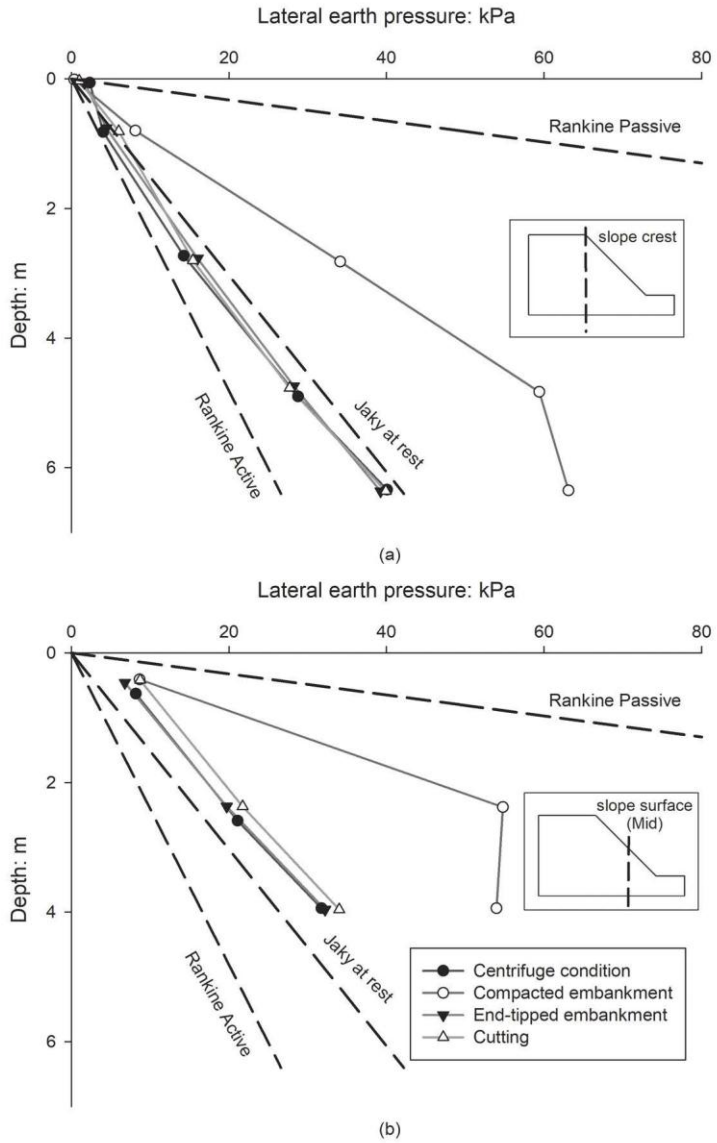

KnappettFig15.TIF

Accepted manuscript doi:
10.1680/jgeot.17.p.128

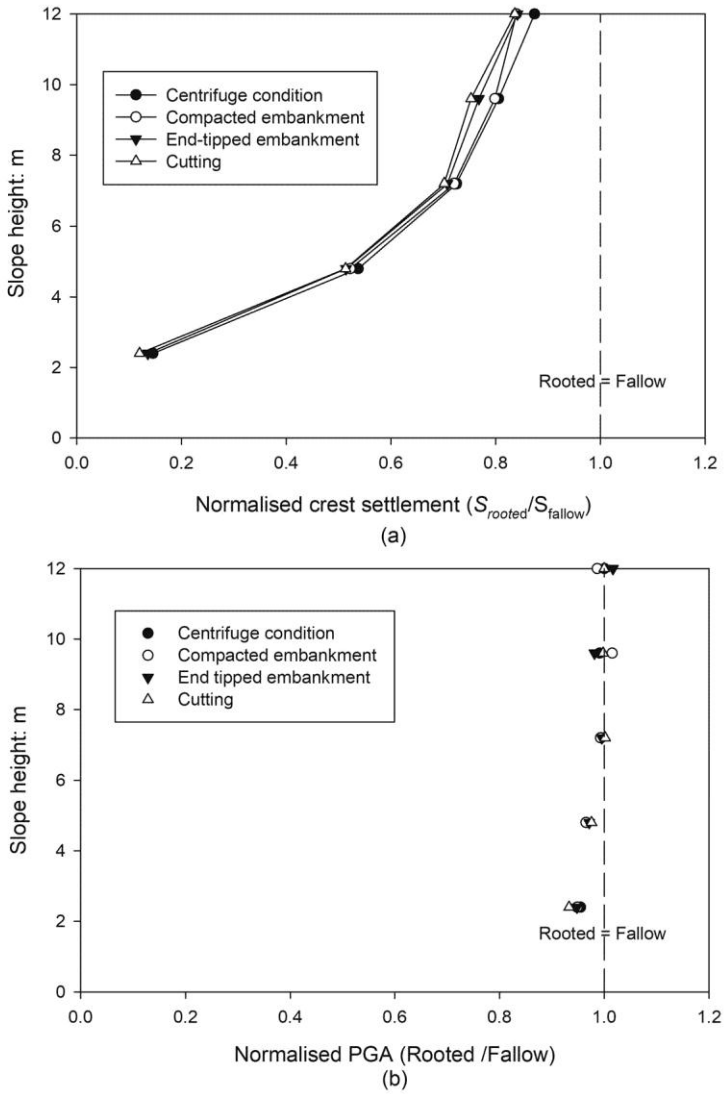

KnappettFig16.TIF

Accepted manuscript doi:
10.1680/jgeot.17.p.128

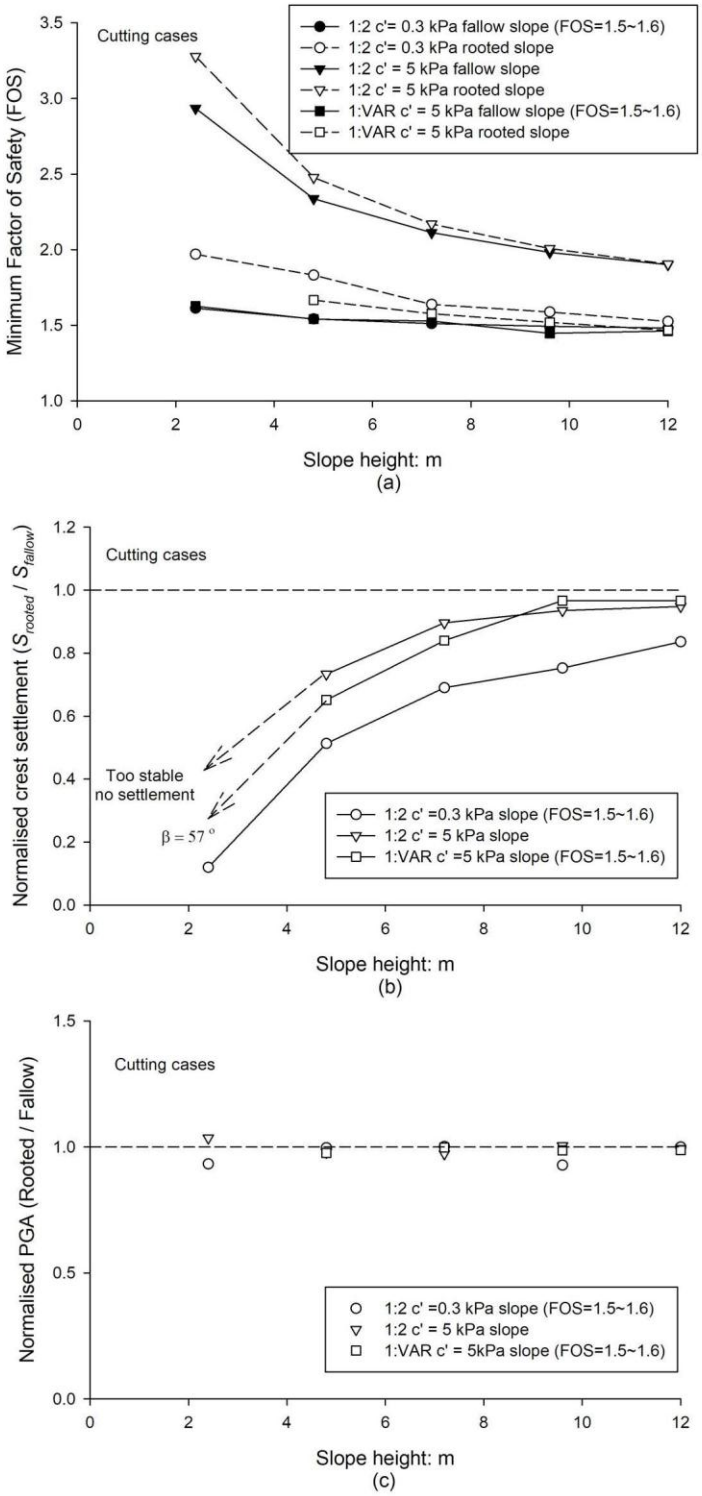

KnappettFig17.tif